

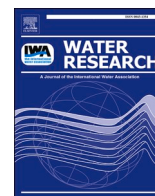
<https://doi.org/10.1016/j.watres.2022.118650>

This item is likely protected under Title 17 of the U.S. Copyright Law. Unless on a Creative Commons license, for uses protected by Copyright Law, contact the copyright holder or the author.

Access to this work was provided by the University of Maryland, Baltimore County (UMBC) ScholarWorks@UMBC digital repository on the Maryland Shared Open Access (MD-SOAR) platform.

Please provide feedback

Please support the ScholarWorks@UMBC repository by emailing scholarworks-group@umbc.edu and telling us what having access to this work means to you and why it's important to you. Thank you.



Photocatalytic degradation of GenX in water using a new adsorptive photocatalyst

Yangmo Zhu^a, Haodong Ji^b, Ke He^c, Lee Blaney^c, Tianyuan Xu^{d,*}, Dongye Zhao^{a,*}

^a Department of Civil & Environmental Engineering, Auburn University, Auburn, AL 36849, USA

^b School of Environment and Energy, Peking University Shenzhen Graduate School, Shenzhen 518055, China

^c Department of Chemical, Biochemical, and Environmental Engineering, University of Maryland Baltimore County, MD 21250, USA

^d School of Resource and Geosciences, China University of Mining and Technology, Xuzhou, Jiangsu 221116, China

ARTICLE INFO

Keywords:

GenX
Adsorptive photocatalyst
Adsorption
Photocatalysis
Defluorination
PFAS

ABSTRACT

GenX, the ammonium salt of hexafluoropropylene oxide dimer acid, has been used as a replacement for perfluorooctanoic acid. Due to its widespread uses, GenX has been detected in waters around the world amid growing concerns about its persistence and adverse health effects. As relevant regulations are rapidly evolving, new technologies are needed to cost-effectively remove and degrade GenX. In this study, we developed an adsorptive photocatalyst by depositing a small amount (3 wt.%) of bismuth (Bi) onto activated-carbon supported titanate nanotubes, Bi/TNTs@AC, and tested the material for adsorption and subsequent *solid-phase* photodegradation of GenX. Bi/TNTs@AC at 1 g/L was able to adsorb GenX (100 µg/L, pH 7.0) within 1 h, and then degrade 70.0% and mineralize 42.7% of pre-sorbed GenX under UV (254 nm) in 4 h. The efficient degradation also regenerated the material, allowing for repeated uses without chemical regeneration. Material characterizations revealed that the active components of Bi/TNTs@AC included activated carbon, anatase, and Bi nanoparticles with a metallic Bi core and an amorphous Bi₂O₃ shell. Electron paramagnetic resonance spin-trapping, UV-vis diffuse reflectance spectrometry, and photoluminescence analyses indicated the superior photoactivity of Bi/TNTs@AC was attributed to enhanced light harvesting and generation of charge carriers due to the UV-induced surface plasmon resonance effect, which was enabled by the metallic Bi nanoparticles. •OH radicals and photogenerated holes (h⁺) were responsible for degradation of GenX. Based on the analysis of degradation byproducts and density functional theory calculations, photocatalytic degradation of GenX started with cleavage of the carboxyl group and/or ether group by •OH, h⁺, and/or e_{aq}⁻, and the resulting intermediates were transformed into shorter-chain fluorochemicals following the stepwise defluorination mechanism. Bi/TNTs@AC holds the potential for more cost-effective degradation of GenX and other per- and polyfluorinated alkyl substances.

1. Introduction

Per- and polyfluorinated alkyl substances (PFAS) are a diverse group of organic chemicals with an aliphatic carbon backbone, where all or most of the C-H bonds are replaced with C-F bonds. The highly polarized and stable C-F bonds (531.5 kJ/mol) make these chemicals thermally and chemically stable and unreactive (Yang et al. 2015). Because of the unique properties, PFAS have been used in a wide array of commercial and industrial products or processes (Rahman et al. 2014; Wang et al. 2015). Currently, more than 4000 PFAS are available on the global market (Lenka et al. 2021). Consequently, PFAS have been widely detected in the aquatic systems. Perfluorooctanoate (PFOA) and

perfluorooctanesulfonate (PFOS) have been of particular concern due to widespread occurrence in water bodies, adverse health effect, and resistance to conventional water treatment processes (Cui et al. 2018; Lindstrom et al. 2011).

Human exposure to PFOA and PFOS has been linked to cancer, elevated cholesterol, immune suppression, and endocrine disruption (Li et al. 2020a). The health concerns prompted manufacturers in Europe and North America to replace PFOA and PFOS with shorter-chain PFAS in the early 2000s (Sunderland et al. 2019). The most notable substitute is the chemical known as GenX, which is also known as hexafluoropropylene oxide dimer acid (HFPO-DA) or perfluoro-2-propoxypropanoic acid (PFPrOPrA). GenX was introduced

* Corresponding authors.

E-mail addresses: xutianyuan@cumt.edu.cn (T. Xu), zhaodong@auburn.edu (D. Zhao).

<https://doi.org/10.1016/j.watres.2022.118650>

Received 9 March 2022; Received in revised form 19 May 2022; Accepted 21 May 2022

Available online 23 May 2022

0043-1354/© 2022 Elsevier Ltd. All rights reserved.

in 2009 by DuPont de Nemours, Inc. In addition, from 2003 on, 3M Company replaced PFOS with perfluorobutanesulfonate (PFBS) in several of its major products (Christensen et al. 2019).

As regulatory actions have been focused on the legacy PFAS (PFOA and PFOS), the use of short-chain substitutes has become a norm in the global fluoropolymer industry. The European Union produced 10–100 tons of GenX per year (Heydebreck et al. 2015). Consequently, GenX has been increasingly detected in waters since 2015 at levels from tens of ng/L to 4.5 µg/L and, in many cases, GenX became the predominant PFAS (Brandma et al. 2019; Heydebreck et al. 2015). Likewise, PFBS was detected in drinking water at concentrations as high as 0.3 µg/L (MDH, Minnesota Department of Health 2017).

While GenX was thought to be a “sustainable replacement” for PFOA, some recent studies have raised growing concerns about its potential adverse effects. Gomis et al. (2018) reported that GenX showed higher toxicity for male rats than PFOA. Wang et al. (2017) observed that exposure to HFPO-DA (1 mg/kg body weight) induced more extensive hepatomegaly for mice than PFOA. The latest assessment from the U.S. Environmental Protection Agency (US EPA) reported a safe daily ingestion level of 3×10^{-6} mg GenX per kg body weight, which is lower than the 2018 level by a factor of 2.7 (THE HILL 2021).

GenX has been widely detected in rivers impacted by fluorochemical plants in the Netherlands, Germany, China, and United States, with the highest concentrations at 812, 86.1, 3100, and 4500 ng/L, respectively (Brandma et al. 2019; Gebbink et al. 2017; Heydebreck et al. 2015; Sun et al. 2016). The GenX concentrations in these drinking water sources far exceeded the US EPA’s lifetime health advisory level of 70 ng/L for the sum of PFOA and PFOS in drinking water (EPA 2016a; 2016b). A recent study reported that GenX was detected in 659 out of 837 private wells surrounding a fluorochemical manufacturing facility in North Carolina, with the maximum GenX concentration reaching 4000 ng/L, and GenX in 207 wells exceeded the State’s provisional drinking water health goal of 140 ng/L (DEQ, North Carolina Department of Environmental Quality 2018).

To mitigate human exposure, researchers have tested various technologies to remove or degrade GenX in drinking water. For example, Dixit et al. (2021) reported that 221 g/L of a strong base anion-exchange resin (Purolite® A860) was able to decrease GenX levels from 10 µg/L to < 10 ng/L. Wang et al. (2019) compared adsorption of GenX by activated carbon (AC) and ion-exchange resins and found that the IRA67 resin offered ~4 times greater capacity than the best AC tested. Mantripragada et al. (2021) observed that functionalized nanofibers provided a maximum GenX removal capacity of ~0.6 mmol/g. While these adsorbents could physically remove GenX, they do not degrade the chemical. Moreover, the regeneration of these rather expensive materials requires toxic, volatile, and costly solvents, such as methanol, and generates large amounts of toxic spent regenerant that requires additional handling and disposal (Xu et al. 2020a).

Destructive techniques, such as advanced oxidation and reduction processes, have also been investigated in recent years (Bao et al. 2018; Olvera-Vargas et al. 2021; Pica et al. 2019). Bao et al. (2018) reported that nearly complete GenX was reductively degraded after 2 h in a UV/sulfite system and >90% of fluoride ions were recovered after 6 h. Pica et al. (2019) reported that boron-doped diamond anodes were capable of degrading 60% of GenX (4.98 mg/L) in nanofiltration retentate within 4 h, and Olvera-Vargas et al. (2021) found that >90% GenX was mineralized by electro-Fenton paired with boron-doped diamond. Information has been very limited on photocatalytic degradation of GenX using heterogeneous photocatalysts. In a recent work that primarily targeting PFOA, Duan et al. (2020) observed that about 16% of GenX ($C_0 = 50$ mg/L, pH = 3.0) was degraded after 120 min of UV (254 nm) irradiation and in the presence of boron nitride. In addition, current photocatalytic practices have been limited to treating bulk water by irradiating large volumes of water-photocatalysts mixtures, which is not only energy intensive, but also requires large-volume reactors and equipment. Due to the high capital and operation costs (Herkert et al.

2020), these technologies may be feasible to degrade high concentrations of PFAS, but less practical for treatment of large volumes of water containing low concentrations of PFAS.

In a previous work, we developed AC-supported titanate nanotubes (TNTs@AC) through a hydrothermal treatment approach using commercially available AC and TiO₂ (Liu et al. 2016). TNTs@AC was able to pre-concentrate low concentrations of phenanthrene onto the photoactive surface heterojunctions and, subsequently, degrade the chemical. Such adsorptive photocatalysts enable a novel “concentrate-&-destroy” strategy, where the target PFAS are pre-concentrated from a large volume of water onto a small volume of a photocatalyst, and then degraded by irradiation of the PFAS-bearing solid particles. Namely, instead of applying UV irradiation to a large volume of raw water, only a small volume of the solids is subjected to UV light, resulting in a significant energy saving. However, plain TNTs@AC bear with some critical drawbacks for the treatment of PFAS (Li et al. 2020a), including (1) the negative surface potential of TNTs leads to unfavorable adsorption of PFAS anions, and (2) the relatively low separation efficiency of photoinduced electron-hole (e^-/h^+) pairs renders limited photoactivity for both legacy and emerging PFAS, although detailed information has yet to be explored.

To improve the performances for PFOA and PFOS, we doped TNTs@AC with a small fraction of Fe and Ga, respectively. In particular, Li et al. (2020a) modified TNTs@AC with 1 wt.% of Fe²⁺ (1 g/L, pH 3.0) and found that the dopant not only facilitated a heads-on adsorption mode of PFOA, but also enhanced the subsequent photocatalytic degradation of PFOA, with >90% of pre-adsorbed PFOA degraded and ~62% mineralized in 4 h under UV (254 nm) irradiation. More recently, Zhu et al. (2021) developed a Ga-doped TNTs@AC and found the composite was able to completely adsorb PFOS within 10 min and defluorinate ~66.2% of the pre-sorbed PFOS after 4 h of the UV irradiation. These prior studies also revealed that the different metal dopants resulted in different material structure and photocatalytic properties and reaction mechanisms. For example, the introduction of Ga created oxygen vacancies that facilitated separation of e^-/h^+ pairs and generation of O₂^{•−} radicals, which effectively degraded PFOS, while Fe-doping caused direct decarboxylation of PFOA by h^+ and generation of •OH radicals. However, our preliminary tests showed that Fe- or Ga-doped TNTs@AC photocatalysts were less effective for GenX degradation and defluorination.

Bismuth-based photocatalysts have been found effective for degrading persistent organic pollutants (POPs), including PFAS (Dong et al. 2015; Weng et al. 2013). Song et al. (2017) reported that BiOCl nanosheets were able to defluorinate 59.3% of PFOA after 12 h of UV irradiation, and the degradation rate was 1.7 and 14.6 times faster than that of commercial In₂O₃ and TiO₂, respectively. Yang et al. (2021) prepared Bi₅O₇I/ZnO heterojunction microspheres and found the material degraded 91% of PFOA after 6 h of visible light irradiation owing to heterojunction structures formed upon calcination at 400 °C, which also extended the photo-response to the visible light region and increased the separation efficiency of e^-/h^+ pairs.

Metallic Bi can also act as an excellent cocatalyst to facilitate charge-carrier separation of Bi³⁺-based photocatalysts (Dong et al. 2014a; Dong et al. 2015), although its role has not been explored for photocatalytic degradation of PFAS. Dong et al. (2015) investigated a semi-metal-organic Bi-g-C₃N₄ nanohybrid, which showed some unique visible light photocatalytic properties when used for NO removal. The superior photoactivity was ascribed to the surface plasmonic resonance (SPR) endowed by Bi metal to enhance visible light harvesting and charge separation. While these works have revealed the potential of Bi⁰-Bi³⁺-based photocatalysts, especially the SPR-enhanced photocatalytic activity, these materials have not been explored for treatment of PFAS.

The overall goal of this study was to develop and test an adsorptive photocatalyst, Bi/TNTs@AC, for enhanced adsorption and subsequent degradation of GenX in water. The specific objectives were to (1)

synthesize the desired catalyst through a two-step hydrothermal-calcination method, (2) measure the adsorption kinetics and capacity of Bi/TNTs@AC for GenX, (3) evaluate the material stability and reusability, and (4) elucidate the reaction pathway and the underlying mechanisms for the enhanced photocatalytic activity through detailed material characterization and density functional theory (DFT) calculations.

2. Materials and methods

2.1. Chemicals and materials

Nano-TiO₂ (Degussa P25) (Evonik, Germany) consisted of anatase (80 wt.%) and rutile (20 wt.%). Filtrosorb-400® granular activated carbon (F-400 GAC) was purchased from Calgon Carbon Corporation (Pennsylvania, USA). Bismuth nitrate pentahydrate (Bi(NO₃)₃·5H₂O) (purity ≥ 98%), sodium hydroxide (NaOH) (≥97%), methanol (CH₃OH) (≥99.8%), isopropyl alcohol (IPA) (70%), benzoquinone (BQ) (99%), sodium azide (NaN₃) (≥99.7%), ethylenediaminetetraacetic disodium salt (EDTA) (99%), and GenX in the form of undecafluoro-2-methyl-3-oxahexanoic acid (97%) were acquired from VWR International (Radnor, PA, USA). Table S1 of the Supplementary Material (SM) presents the salient properties of GenX. Analytical standards of HFPO-DA and its mass labeled compound, 2,3,3,3-tetrafluoro-2-(1,1,2,2,3,3,3-heta-fluoropropoxy)-¹³C₃-propanoic acid (M3HFPO-DA), which was used as an internal standard (IS), were purchased from Wellington Laboratories Inc. (Guelph, Ontario, Canada). All solutions were prepared using deionized (DI) water (18.2 MΩ cm).

2.2. Preparation of Bi/TNTs@AC

First, TNTs@AC was synthesized through a modified, one-step, hydrothermal method (Liu et al. 2016; Ma et al. 2017). Typically, 1.2 g of GAC and 1.2 g of TiO₂ were added to 66.7 mL of a 10 M NaOH solution and stirred for 12 h. The mixture was transferred into a 100 mL Teflon reactor enclosed in a stainless-steel cup and heated in an oven at 130 °C for 72 h. Two distinct layers were observed after gravity settling for 1 h. The upper layer was removed, whereas the bottom black precipitate (TNTs@AC) was washed with DI water until the water pH reached 7.0 ± 0.5, and then oven-dried at 105 °C for 8 h. Upon proper grinding and sieving, the particles in the size range of 150–425 μm were used in the subsequent experiments. No fluorine or fluoride was detected in the resulting material.

Furthermore, 1 g of the prepared TNTs@AC was dispersed in 80 mL DI water. Separately, 1.16 g Bi(NO₃)₃·5H₂O (5 g/L as Bi) was dissolved in a solution consisting of 20 mL of concentrated HNO₃ and 80 mL of DI water. Then, a known volume (i.e., 2, 4, 6, 8, and 10 mL) of the Bi(NO₃)₃·5H₂O solution was added dropwise into the TNTs@AC suspension. The mixtures were equilibrated under stirring for 3 h, at which nearly all Bi³⁺ was adsorbed on TNT (Ti-O⁻). Upon separation of the solids, the supernatant was analyzed for residual Ti and Bi. In all cases, <0.01% of Ti and <0.01% of Bi were detected in the supernatant. The Bi-loaded TNTs@AC was dried at 105 °C for 8 h, and the resulting particles were calcined at 550 °C for 3.5 h in a nitrogen atmosphere with a temperature ramp of 10 °C/min and a nitrogen flow of 2.5 L/min. The mass ratio of Bi to TNTs@AC was controlled at 1, 2, 3, 4, and 5 wt.%, and the corresponding composites were denoted as 1%Bi/TNTs@AC, 2%Bi/TNTs@AC, 3%Bi/TNTs@AC, 4%Bi/TNTs@AC, and 5%Bi/TNTs@AC, respectively. To inform the performance of the composite materials, treated AC, TNTs@AC, and 3%Bi/TNTs were also prepared via the same procedure.

2.3. Material characterization

The properties of the crystal phases were analyzed using a Bruker D2 Phaser X-ray diffractometer (XRD) (Bruker AXS, Germany) with Cu Kα radiation (λ, 1.5418 Å). The surface morphology and elemental

composition were examined by scanning electron microscopy (SEM, SU8010, Hitachi, Japan) equipped with energy-dispersive X-ray spectroscopy (EDS). The microstructural characteristics were analyzed by high-resolution transmission electron microscopy (HRTEM, JEOL, JEM-2100F, Japan). The elemental compositions and oxidation states were determined via X-ray photoelectron spectroscopy (XPS, Thermo Scientific K-Alpha, UK) with Al Kα X-Ray Irradiation at 15 kV and 15 mA. The standard C1s peak (binding energy, 284.8 eV) was used to calibrate the XPS peaks and eliminate static charge effects. An etching technique was used to analyze the depth profile using a monoatomic Ar ion gun (energy: 1000 eV; raster size: 1 × 1 mm). The etching depths were 50 and 150 nm for the XPS analyses, corresponding to an etching time of 250.4 s and 751.2 s, respectively. The N₂ Brunauer-Emmett-Teller (BET) specific surface area (SSA) and pore volume of the materials were analyzed through the nitrogen adsorption-desorption procedure (Micromeritics ASAP 2460, USA). The pore size distribution was obtained following the Barret-Joyner-Halender (BJH) method. Zeta potential was determined by a Nano-ZS90 Zetasizer (Malvern Instruments, UK). The electronic properties were measured through the electron paramagnetic resonance (EPR) method using a Bruker EMXPLUS spectrometer. The photoluminescence (PL) spectra were obtained from an FLS1000 photoluminescence spectrometer (Edinburgh Instruments, UK) equipped with a xenon source at an excitation wavelength of 254 nm. The UV-vis diffuse reflectance spectrometry (UV-DRS) analysis was performed on a Shimadzu UV-3600i Plus spectrophotometer.

2.4. Adsorption kinetic and isotherm tests

Adsorption kinetic experiments were conducted in 45 mL high-density polypropylene (HDPE) vials. To facilitate the chemical analysis and evaluation of material effectiveness, the experimental solutions were prepared with an initial GenX concentration of 100 μg/L. The adsorption was initiated by adding 0.04 g Bi/TNTs@AC to 40 mL of a 100 μg/L GenX solution with an initial pH of 7.0 ± 0.1. The vials were placed on a rotator (70 rpm) at 25 °C in the dark. Duplicate vials were sacrificially sampled at predetermined times. Upon filtering through a 0.22 μm polyether sulfone (PES) membrane, the filtrates were analyzed for GenX remaining.

Adsorption isotherms were measured in a similar manner, but the mixtures were equilibrated for 24 h to ensure equilibrium. The initial GenX concentration was varied (i.e., 0.1, 0.4, 1, 3, 5, 20, 50, 80, 100 mg/L), while the dosage of Bi/TNTs@AC was kept at 1 g/L. For comparison, the kinetic and equilibrium isotherm tests were also carried out with treated AC and TNTs@AC following the same experimental protocols. Note, no Bi was detected in the supernatant during the kinetics and isotherm experiments.

2.5. Photodegradation of pre-sorbed GenX

The photocatalytic degradation experiments were carried out in a Rayonet RPR-100 UV-reactor (Southern New England Ultraviolet CO., Branford, CT, USA) equipped with 16 RPR-2537 Å lamps. The system was fan-cooled and maintained at a temperature of ~35 °C. Following the adsorption equilibrium, the GenX-laden Bi/TNTs@AC was separated by gravity settling for 1 h (>99% settled). Subsequently, ~95% of the supernatant was removed, and the remaining solid-liquid mixture was transferred into a quartz tray (OD×H = 6×1.5 cm) with a quartz cover. Then, 8 mL DI water was added to the mixture to achieve a total solution volume of 10 mL. The mixture was placed at the center of the photo-reactor chamber. The light intensity was 210 W/m² at the edge (1.5 in or 3.81 cm to the nearest lamp) of the quartz tray and 128 W/m² at the center. At predetermined times (i.e., 1, 2, 3, and 4 h), the mixtures were sacrificially filtered through a 0.22-μm PES membrane (>99% GenX recovery), and the filtrates analyzed for GenX and fluoride. To measure the residual solid-phase GenX concentration, the solids were extracted using 20 mL methanol at 80 °C for 4 h in a water bath. After

centrifugation at 2500 rpm for 5 min, the supernatant was transferred to a clean vial, and then the solids were extracted with another 20 mL of methanol under the same conditions. The extractants were then combined and analyzed for GenX. The total GenX recovery was >95%, and thus no surrogate IS was used during the extraction. No fluoride was detected when the solids were washed with 20 mL of a 1 M NaOH solution.

The effect of catalyst dosage on the photodegradation effectiveness were carried out following the same experimental protocol, but the material dosage was varied from 1 to 5 g/L.

2.6. pH effect

To evaluate effect of solution pH on the adsorption process, experiments were conducted with 3%Bi/TNTs@AC (the best performing material) at a dose of 1 g/L and an initial GenX concentration of 100 µg/L. The equilibrium solution pH was 3.5 ± 0.1 , 5.0 ± 0.1 , 7.0 ± 0.1 , 8.5 ± 0.1 , and 10.0 ± 0.1 . To determine the impact of pH on GenX photodegradation, the pH in the adsorption stage was set at 7.0 ± 0.1 (material dosage = 2 g/L, initial GenX = 100 µg/L), while the pH during the photodegradation was varied from 3.5 ± 0.1 to 10.0 ± 0.1 .

2.7. Material stability and reusability

3%Bi/TNTs@AC was subjected to five consecutive cycles of adsorption and photodegradation. The same experimental protocols for the adsorption and the subsequent photodegradation were followed, and leaching of Bi and Ti into the aqueous phase was analyzed after each cycle.

2.8. Roles of UV-induced reactive species

The contribution of common UV-induced reactive species to the photocatalytic degradation of GenX was assessed using various scavengers. In particular, EDTA, ISA, BQ, and NaN₃ were added to experimental mixtures to quench photogenerated holes (h^+), hydroxyl radicals ($\cdot\text{OH}$), superoxide radicals ($\text{O}_2^{\cdot-}$), and singlet oxygen ($^1\text{O}_2$), respectively (Van Doorslaer et al., 2012). The same experimental procedures were followed for the adsorption and photodegradation tests except one of the scavengers was present during the photodegradation at various concentrations (0.5, 1.0, 5.0, and 10.0 mM). The use of the molarity units was to facilitate cross-comparison among the scavengers and with literature data for other materials.

2.9. Density functional theory calculations

The Fukui functions, which are based on the density functional theory (DFT), were employed to predict the attack sites in GenX for different radicals using the Gaussian 16 C.01 package (Ji et al. 2020). The geometry optimization and single-point energy calculations were carried out via the B3LYP method with the 6-31+G(d,p) basis set. Section S1 in SM provides more details on the DFT calculations.

2.10. Chemical analysis

Aqueous-phase GenX concentrations were analyzed by a Vanquish Flex Binary UPLC system (Thermo Fisher, USA) coupled with a quadrupole-Orbitrap mass spectrometer (Orbitrap Exploris TM120, Thermo Fisher) using the negative mode electrospray ionization (ESI). A delay column was placed between the pump and autosampler (HypersilGOLD, 1.9 µm, 175 Å, 3 × 50 mm). M3HFPO-DA (20 µg/L) was used as the IS for the analysis. The limit of detection for GenX was 0.5 µg/L. GenX and two potential transformation products, trifluoroacetic acid (TFA) and pentafluoropropionic acid (PFA), were further confirmed by an UltiMate 3000 LC coupled to a Thermo TSQ Quantum Access Max triple quadrupole tandem mass spectrometer. Additional analytical

details are provided in Section S2 of the SM. Fluoride was analyzed by ion chromatography (Dionex, CA, USA) equipped with an anion-exchange column (Dionex Ionpac AS22) and an anion dynamically regenerated suppressor (ADRS 600, 4mm). The detection limit was 10.00 ± 0.01 µg/L. Dissolved Bi and Ti were measured by inductively coupled plasma-optical emission spectroscopy (ICP-OES, 710-ES, Varian, USA), with a detection limit of 100 µg/L and 50 µg/L, respectively.

3. Results and discussion

3.1. Material phases and chemical composition

Fig. 1a shows the XRD patterns of calcined TNTs@AC and Bi/TNTs@AC loaded with 1-5 wt.% Bi. For TNTs@AC, the diffraction peaks at 10.5° , 24.4° , 28.4° , and 47.8° are assigned to sodium tri-titanate with a chemical formula of $\text{Na}_x\text{H}_{2-x}\text{Ti}_3\text{O}_7$ (x depends on the sodium content) (Wang et al. 2018). The basic skeleton of tri-titanate was composed of edge-sharing triple $[\text{TiO}_6]$ octahedrons with Na^+ and H^+ attached at the interlayers as exchangeable counter ions (Ma et al. 2017). The intensity of the diffraction peaks of TNTs@AC were notably decreased compared to those of uncalcined TNTs@AC and uncalcined 3%Bi/TNTs@AC (Fig. S1), which can be attributed to breakage of the tubular and layered structures during calcination (Razali et al. 2012), partial collapse of polymerized Ti species (Ti-O-Ti species), and/or decrease in isolated Ti species with higher coordination numbers (Yang and Li 2002). Moreover, the XRD diffraction pattern for calcined TNTs@AC showed a red shift compared to that of uncalcined TNTs@AC (e.g., from $\sim 9.8^\circ$ to 10.5°) (Fig. S1), indicating a decrease in interlayer distance due to the release of water molecules (Qamar et al. 2008). Compared to calcined TNTs@AC and uncalcined Bi/TNTs@AC, the XRD patterns for calcined Bi/TNTs@AC with different Bi contents displayed five characteristic peaks with 2θ values of 25.3° , 37.8° , 48.1° , 54.2° , and 62.2° corresponding to the (101), (004), (200), (211), and (213) planes of tetragonal anatase (JCPDS-ICDD No. 21-1272), respectively. This result indicates that sodium tri-titanate was transformed into anatase due to Bi doping and calcination. The adsorption of Bi^{3+} ions on TNTs@AC partially replaced Na^+ ions, which is conducive to the formation of anatase upon calcination (Cai et al. 2017, Lee et al. 2007). In addition, for Bi/TNTs@AC (Fig. 1a), the characteristic peaks at 22.5° , 27.2° , 39.6° , 44.6° , 46.0° , 48.7° , 64.5° , and 70.8° confirmed the existence of the rhombohedral phase of metallic Bi (JCPDS-ICDD No. 44-1246). In contrast, no evidence of metallic Bi peaks was observed for uncalcined Bi/TNTs@AC (Fig. S1), indicating that the calcination facilitated the reduction of Bi^{3+} into Bi^0 . The XPS analysis confirmed that Bi^{3+} on TNTs@AC was reduced into Bi^0 with AC as the electron donor at 550°C .

Fig. 1a also indicates that increasing the Bi content from 1 wt.% to 3 wt.% enhanced the peak intensities of Bi, whereas further increasing Bi to 4 and 5 wt.% resulted in a lower Bi intensity. Accordingly, 3%Bi/TNTs@AC demonstrated the highest GenX defluorination efficiency (Section 3.4) and was, therefore, selected for further testing.

XPS spectra were obtained to examine the chemical composition of Bi/TNTs@AC and TNTs@AC. The scans were performed in two ways, one on the pristine material surface and the other after Ar-ion etching at depths of 50 and 150 nm. Fig. S2a confirms the presence of Ti, C, Na, O, and Bi on the 3%Bi/TNTs@AC surface. For the spectra of Bi 4f without etching (Fig. 1b), the peaks centered at 164.0 and 158.7 eV are characteristic of Bi^{3+} in bismuth oxides and are ascribed to $\text{Bi } 4f_{5/2}$ and $\text{Bi } 4f_{7/2}$, respectively (Lan et al. 2020). In conjunction with the XRD results, which showed no crystalline Bi_2O_3 on Bi/TNTs@AC, the Bi_2O_3 identified by XPS was amorphous.

The two Bi 4f peaks in Fig. 1b shifted from 164.0/158.7 eV to lower binding energies of 163.9/158.6 eV with 50 nm etching and 163.6/158.4 eV with 150 nm etching. These results can be attributed to the partial reduction of Bi^{3+} species (Liu et al. 2017). Two additional peaks were present at 161.6 and 156.3 eV after the 50 nm etching, and these peaks were attributed to Bi-Bi bonds and confirmed the presence of

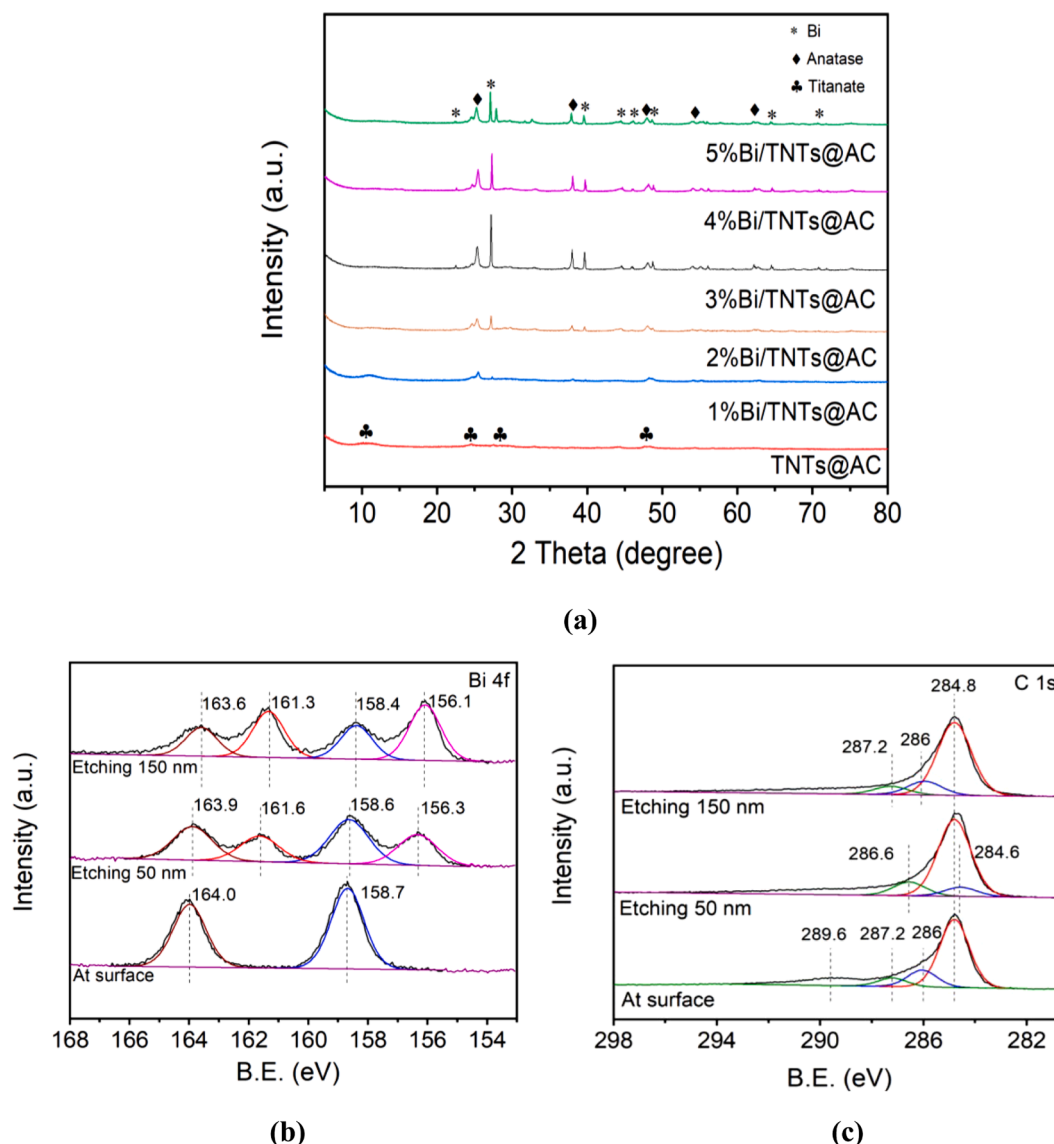


Fig. 1. (a) XRD patterns of TNTs@AC and Bi/TNTs@AC prepared with 1-5 wt.% Bi, (b) high-resolution XPS spectra of Bi 4f for 3%Bi/TNTs@AC, and (c) high-resolution XPS spectra of C 1s at the surface before and after etching. TNTs@AC and 3%Bi/TNTs@AC were calcined at 550 °C in all cases.

metallic Bi in the composite (Yang et al. 2020). The Bi-Bi peak intensity was stronger for the 150 nm etching, suggesting that more metallic Bi was present in the particle core. Namely, the Bi particles consisted of a metallic Bi core and a thin amorphous Bi_2O_3 shell on the surface of Bi/TNTs@AC.

The binding energies were corrected by the C 1s levels at 284.8 eV as a reference. The C 1s spectra (Fig. 1c) measured at the surface of the pristine sample can be deconvoluted into three peaks corresponding to C-O (286.0 eV), C=O (287.2 eV), and O-C=O (289.6 eV) bonds, which were also present after the 150 nm etching with the exception of O-C=O bonds (Gopiraman et al. 2017). After the 50 nm etching, the oxygenated carbon groups disappeared, and two additional peaks occurred at 284.6 eV and 286.6 eV. The peak at 284.6 eV highlights the existence of C-C groups (Wang et al. 2020), whereas the peak at 286.6 eV was attributed to carbonyl or quinine groups (Ma et al. 2015). In addition, the O 1s XPS spectra (Fig. S2b) highlighted the presence of Bi-O bonds at 529.7 eV and the regular lattice oxygen (Ti-O-Ti) at 531.3 eV (Almeida et al. 1998; Dong et al. 2015). The peaks at 458.2 eV and 464.0 eV in Fig. S2c belong to Ti 2p_{3/2} and Ti 2p_{1/2}, respectively, which are characteristic of Ti⁴⁺ (Li et al. 2020b).

3.2. Morphological characterization

Figs. S3a and S3b show the SEM images of 3%Bi/TNTs@AC calcined at 550 °C, where the surface displayed a flower-like structure with interwoven TNTs grafted on the AC petals. Micro- or nano-AC particles were attached to well-defined TNTs (Figs. 2a and S3b). This observation indicates that the hydrothermal treatment under alkaline conditions not only converted TiO_2 into TNTs, but also altered the structure of the AC, resulting in mutual modification of AC and TNTs. The EDS mapping (Figs. S3c and S3d) revealed that five major elements (*i.e.*, C, O, Ti, Na, and Bi) were uniformly distributed on 3%Bi/TNTs@AC, and Table S3 presents the percentile of each element. The high Ti (36.2%), C (19.2%), and Bi (5.2%) contents corroborate the formation of Bi/TNTs@AC.

Figs. 2a-2c present the TEM images of 3%Bi/TNTs@AC. Fig. 2a confirms the hybridization of TNTs and AC nanoparticles. The coated carbon particles on TNTs are beneficial and facilitate hydrophobic interactions with GenX and anion- π interactions between GenX and the electron-deficient aromatic skeletons of AC. The interlayer distance of TNTs was 0.75 nm (Fig. 2c), which agrees with the crystal plane (020) of titanate (Wang et al. 2018), whereas the lattice fringe spacing of 0.35 nm (Fig. 2b) conforms to the (101) plane of anatase. Prior work on

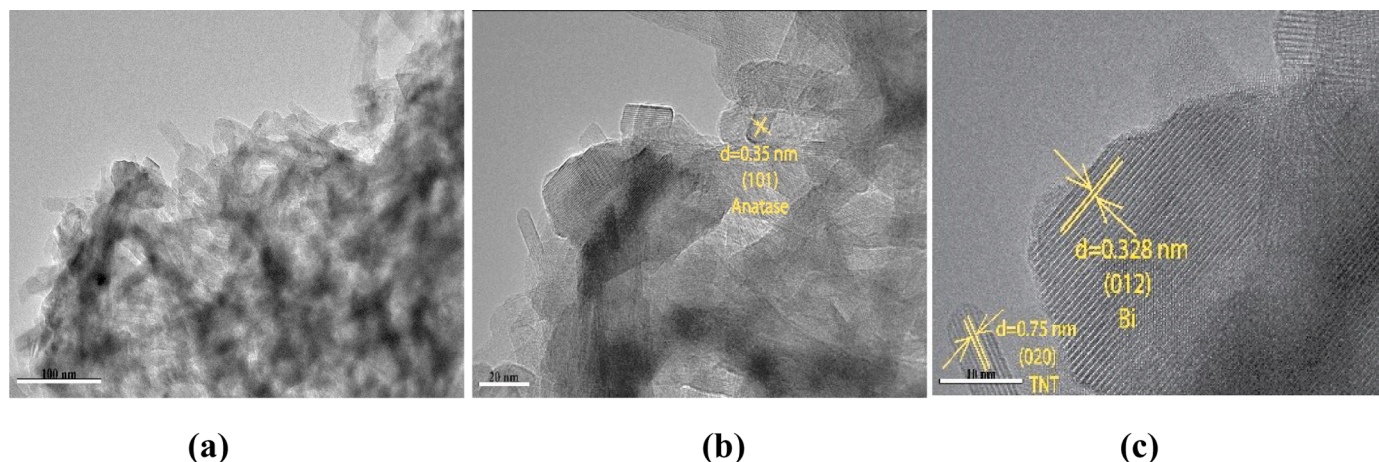


Fig. 2. (a, b, c) TEM and HRTEM images of 3%Bi/TNTs@AC calcined at 550 °C. Scale bars are equivalent to 100, 20, and 10 nm, respectively.

TNTs@AC showed that no transformation from tri-titanate to anatase would occur upon calcination without a metal dopant (Zhu et al. 2021). This observation suggests that Bi on TNTs facilitated transformation from titanate to anatase, while TNTs retained its nanotube structure

with an inner diameter of ~ 5 nm and an outer diameter of ~ 12 nm (Fig. 2c). In addition, the lattice spacing (0.328 nm) shown in Fig. 2c corresponds to the (012) lattice plane of metallic Bi (Dong et al. 2015), which is expected to facilitate electron transfer and inhibit

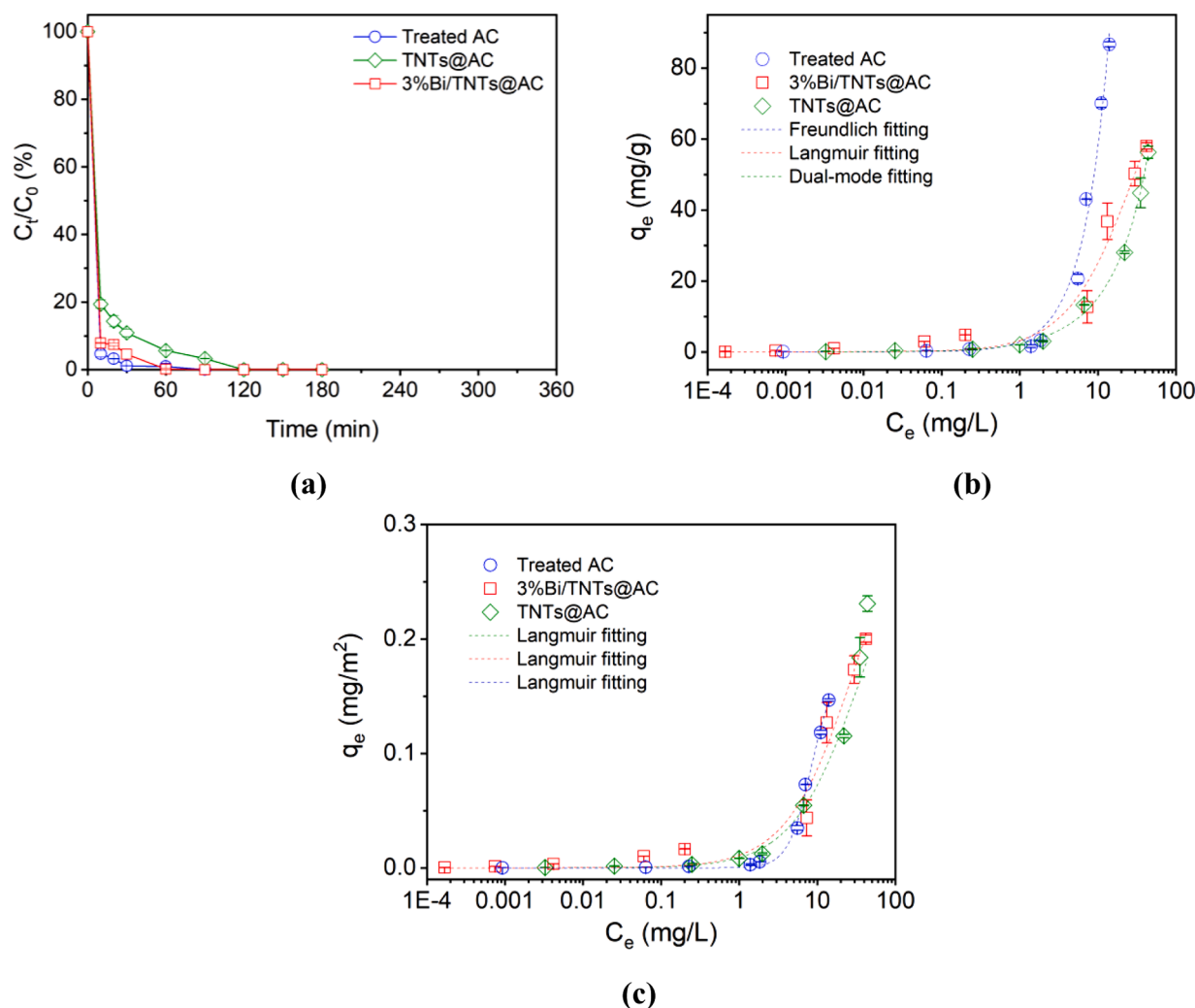


Fig. 3. (a) Adsorption kinetics and equilibrium isotherms based on (b) unit-mass uptake and (c) unit surface-area uptake of GenX by treated AC, TNTs@AC, and 3% Bi/TNTs@AC. Experimental conditions for kinetic tests—Initial GenX concentration = 100 $\mu\text{g/L}$, material dosage = 1 g/L, pH = 7.0 ± 0.1 ; Conditions for isotherm experiments—Initial GenX concentration = 0.1–100 mg/L, material dosage = 1 g/L, pH = 7.0 ± 0.1 . Data are plotted as mean of duplicates with error bars indicating relative deviation from the mean.

recombination of electron-hole pairs (Section 3.4).

Fig. S4a shows the N₂ adsorption-desorption isotherms of TNTs@AC and Bi/TNTs@AC with 1-5 wt.% Bi. According to the International Union of Pure and Applied Chemistry (IUPAC) classification system, all isotherms are Type IV and characteristic of mesoporous materials. In the low P/P_0 range, the shape of the isotherms conformed to monolayer-multilayer adsorption. Subsequently, the H3 type hysteresis loops appeared at around $P/P_0 = 0.40$, suggesting that another adsorption mechanism, such as capillary condensation, occurred in the nanotubes and/or mesoporous channels (Liu et al. 2016). When the Bi content was increased from 1 to 5 wt.%, the hysteresis loop became larger, which aligns with the capillary condensation mechanism (El-Sheikh et al. 2017). Fig. S4b gives the pore size distribution determined using the BJH method. Except for TNTs@AC and 3%Bi/TNTs@AC, the pore size distributions displayed a bimodal profile with major peaks at 3.7 nm and minor peaks at 8.9-16.0 nm. 3%Bi/TNTs@AC showed the most uniform pore size distribution of the Bi-doped composites. Table S4 summarizes the SSA and pore volume for all materials. The SSA of TNTs@AC was 243.77 m²/g, which is lower than that for the AC by a factor of 2.4, indicating partial blockage of the internal pores (pore volume also decreased by 2.4×) upon the loading of TNTs. When loaded with 1, 2, 3, 4, and 5 wt.% of Bi, the SSA was increased from 243.77 m²/g for TNTs@AC to 307.50, 279.60, 289.84, 285.26, and 269.78 m²/g, respectively. The increase in SSA stemmed from pore volume increases (Table S4) resulting from the Bi-mediated phase transformation and restructuring of TNTs and AC (Fig. S3) (Subramaniam et al. 2017). Excessive Bi doping resulted in a slight decrease in SSA due to the increased crystal sizes of anatase and metallic Bi, which partially blocked nanopores (Table S5) (Zhong et al. 2012). The newly created sites associated with the elevated SSA are expected to not only facilitate GenX adsorption, but also be more photoactive due to the hybridization of Bi, TNTs, and AC.

3.3. GenX adsorption kinetics and isotherms

Fig. 3a compares the GenX adsorption kinetics of 3%Bi/TNTs@AC and its precursor materials, AC and TNTs@AC, which were subjected to the same hydrothermal treatment and calcination process. The rate of GenX adsorption by 3%Bi/TNTs@AC was nearly the same as that of the treated AC on an equal mass basis (40 mg), and >99% of GenX was removed in 1 h with >90% of the removal occurred in the first 10 min. TNTs@AC showed a slower adsorption rate, and equilibrium was not reached until 120 min due to the poor affinity of GenX to the negatively charged TNTs. Fig. S5 shows that when the material dosage was halved to 20 mg, 3%Bi/TNTs@AC displayed clearly faster adsorption rate than the treated AC. The results confirmed that the Bi loading notably improved the adsorption rate of GenX due to (1) suppression of the negative surface potential of TNTs (the pH_{pzc} of TNTs and 3%Bi/TNTs were 2.6 and 6.3, respectively), and (2) Lewis acid-base interactions between Bi and the carboxylate group of GenX.

The pseudo-first-order Eq. (1) and pseudo-second-order Eq. (2) kinetic models were utilized to interpret the kinetic data:

$$q_t = q_e - q_e \exp(-k_1 t) \quad (1)$$

$$q_t = \frac{k_2 q_e^2 t}{1 + k_2 q_e t} \quad (2)$$

where q_t and q_e (μg/g) are the solid-phase GenX concentrations at time t (min) and equilibrium, respectively, and k_1 (min⁻¹) and k_2 (g/(μg · min)) are the respective rate constants.

Table S6 summarizes the kinetic parameters for both models. The pseudo-second-order model gave a better goodness of fit, as evidence by the $R^2 > 0.99$ for all three materials. However, both models can adequately fit the kinetic data. The different rate constants are in line with the characterization results that the Bi- and TNTs-modifications of

the AC, along with the hydrothermal and calcination treatments, altered accessibility of the adsorption sites.

Because GenX concentrations in industrial and contaminated waters can widely vary, detailed isotherms were constructed for AC and 3%Bi/TNTs@AC over a broad range of equilibrium concentrations, namely 0.1 - 100 mg/L (Fig. 3b). The classical Langmuir Eq. (3) and Freundlich Eq. (4) isotherm models were tested to fit the experimental data:

$$q_e = \frac{Q_{\max} b C_e}{1 + b C_e} \quad (3)$$

$$q_e = K_F C_e^{1/n} \quad (4)$$

where Q_{\max} (mg/g) is the Langmuir maximum capacity, b (L/mg) is the Langmuir affinity coefficient, K_F (mg/g·(L/mg)^{1/n}) is the Freundlich capacity parameter, and n is the heterogeneity factor related to the presence and distribution of different sorption sites.

Table S7 summarizes the parameters for the models. Based on the coefficients of determination (R^2), both models were able to adequately fit the experimental data, though the Freundlich model offered better fitting for AC and TNTs@AC, suggesting a heterogeneous nature in terms of adsorption energy and modes. According to the Langmuir model, the maximum adsorption capacities of GenX on AC, TNTs@AC, and 3%Bi/TNTs@AC were 120.26, 79.96, and 101.77 mg/g, respectively. While the SSA of treated AC was about 2.4 times greater than that of 3%Bi/TNTs@AC, the Langmuir maximum capacity of AC was only ~1.2 times higher. This disproportionality indicates that although the loading of TNTs and Bi on AC resulted in partial loss of the adsorption sites in the core AC, it created a layer of new sites on the AC. The new sites consisted of mixed phases of TNTs, AC particles, and Bi nanoparticles, which enabled a synergized adsorption mechanism and enhanced affinity for GenX. The enhanced affinity of 3%Bi/TNTs@AC for GenX can be well revealed when the isotherm data are plotted based on the surface-area-normalized uptake (Fig. 3c, Table S8), and Fig. S6 shows that the adsorption of GenX by 3%Bi/TNTs@AC was much more favorable in the lower GenX concentration range ($C_e \leq 2$ mg/L) than treated AC and TNTs@AC. The SSA-based Q_{\max} values (mg/m²) followed the order of: 3%Bi/TNTs@AC (0.35) > TNTs@AC (0.33) > AC (0.18). Treated AC offered higher GenX uptake only when the GenX concentration is very high ($C_e > 2$ mg/L) (Fig. 3b) due to its much larger SSA (591.38 m²/g). The enhanced performance of 3%Bi/TNTs@AC can be attributed to synergistic adsorption interactions between anionic GenX and 3%Bi/TNTs@AC (i.e., hydrophobic, Lewis acid-base, and anion-π interactions), whereas only hydrophobic interaction was operative for treated AC and TNTs@AC. Thus, the improved affinity of Bi/TNTs@AC for GenX is expected to not only selectively concentrate GenX on the photoactive surface sites, but also facilitate the subsequent solid-phase photocatalytic degradation of GenX.

Fig. S7 shows the measured zeta potential of 3%Bi/TNTs@AC, which exhibited a pH_{pzc} of ~3.8. Hence, in the circumneutral pH range, the adsorption of GenX anions ($pK_a = 2.8$) by 3%Bi/TNTs@AC would not be favorable due to electrostatic repulsion, although the loading of Bi suppressed the surface negative potential (Fig. S7). While the tail group of GenX is not expected to interact with TNTs ($pH_{pzc} = 2.6$), the Bi deposited on the surface of Bi/TNTs@AC may react with GenX through concurrent electrostatic and Lewis acid-base interactions between Bi³⁺ and the hydrophilic head groups (–COO[–]) of GenX (Khan and Siddiqui 2021; Liu et al. 2015; Liu et al. 2016), which is in line with the strong adsorption observed at neutral pH. The higher GenX adsorption by 3% Bi/TNTs@AC could also be due to the larger SSA resulting from the mixed phases (Section 3.2), which enables hydrophobic reactions between the C-F chain of GenX (except one oxygen atom in the carbon chain) and the AC surface; furthermore, anion-π interactions may also occur between GenX anions and aromatic groups on the AC surface (Xu et al. 2020). The presence of AC and Bi in the composite materials, therefore, enabled cooperative hydrophobic, Lewis acid-base, and

anion- π interactions, not only enhanced the adsorption capacity for GenX, but also facilitated a side-on adsorption mode which is conducive to the *in situ* photochemical degradation of pre-adsorbed GenX (Li et al. 2020a).

3.4. Photodegradation of pre-concentrated GenX on Bi/TNTs@AC

Fig. 4 shows the photocatalytic degradation rates of pre-adsorbed GenX by treated AC, TNTs@AC, and Bi/TNTs@AC with 1–5 wt.% Bi. After 4 h of the UV irradiation, almost no GenX degradation was observed for AC and TNTs@AC. In contrast, Bi/TNTs@AC degraded up to 70.0% of the pre-concentrated GenX, with up to 42.7% defluorinated (i.e., conversion of fluorine into fluoride). Extending the UV irradiation to 6 and 8 h elevated the GenX photodegradation to 75.1% and 77.2%, and mineralization to 45.3% and 46.1%, respectively (Fig. S8). In accord with the material characterization data, 3%Bi/TNTs@AC exhibited the highest photoactivity for GenX. Excessive Bi (i.e., >3 wt. %) may act as recombination centers of the photo-generated electrons and holes.

Fig. 5a shows the effect of catalyst dosage (1, 2, 3, and 5 g/L) during the adsorption stage on the subsequent photodegradation/defluorination of GenX under UV irradiation. Increasing the photocatalyst dosage from 1 to 2 g/L improved the 4-h GenX degradation and defluorination from 70.0% to 74.1% and from 42.7% to 48.3%, respectively. However, further increasing the dosage to 3 or 5 g/L resulted in lower rates of degradation and defluorination, which can be attributed to diminished light penetration as a result of elevated shading effects from denser suspended particles and aggregation of the particles (Ahmadpour et al. 2020; Mirzaei et al. 2018). Consequently, the dosage of 2 g/L was used in the subsequent studies. In practice, the material dosage should be tuned according to the target water quality conditions.

Different catalyst dosages during the adsorption stage result in adsorption of GenX on sites with different accessibility and photoactivity. Kinetically, GenX will be loaded on the more easily accessible sites at higher material doses. From the photoactivity perspective, the hybrid sites with Bi-TNTs-AC are more photoactive, while the pure AC phase may only adsorb but not degrade GenX. While most adsorption sites of AC are located inside the particles, the main adsorption sites for 3%Bi/TNTs@AC are likely to be on the outside shell. The differences in adsorption sites were evidenced by the reduced SSA of 3%Bi/TNTs@AC compared to the parent AC (Table S4). The overall degradation efficiency depends on the fraction of GenX loaded on the more photoactive sites, which are accessible to not only GenX, but also photons,

photogenerated charge carriers, and reactive oxygen species (ROS) (Ding et al. 2013) (Section 3.7). In practice, the low fraction of non-reactive sites should not affect the overall process, because this photo-inert adsorption capacity will remain constant in each treatment cycle and will not affect GenX adsorption and photodegradation on the reactive sites, which are automatically regenerated upon the photodegradation.

3.5. pH effects on GenX adsorption and photodegradation

Fig. 5b shows the effect of pH on GenX adsorption by 3%Bi/TNTs@AC. Nearly all (~99%) of the GenX was consistently adsorbed from the solution over a broad pH range of 3.5–10 upon equilibrium. Due to the low pK_a value (2.8), GenX mainly existed in the anionic form in the pH range tested. In light of the pH_{pzc} of ~3.8 for 3%Bi/TNTs@AC and 6.3 for Bi/TNTs (Section 3.3), a negative overall surface potential would be expected for 3%Bi/TNTs@AC in the experimental pH range (except for pH 3.5), namely, electrostatic interactions between GenX and 3%Bi/TNTs@AC are unfavorable at neutral or alkaline pH. At more alkaline pH, the surface potential of Bi/TNTs turned more negative (pH_{pzc} = 6.3), and thus the interaction with the carboxylate group of GenX became more unfavorable due to electrostatic repulsion and competition of OH^- . Consequently, adsorption of GenX would largely rely on the hydrophobic and anion- π interactions between GenX and AC, resulting in a vertical tail-on orientation adsorption mode (Li et al. 2020a). Conversely, at more acidic pH, adsorption of GenX becomes more favorable for enhanced electrostatic interaction between the positively charged surface of Bi/TNTs and GenX and Lewis acid-base interaction between GenX and the metals (i.e., Bi, Ti). In this case, GenX tends to be adsorbed in the parallel or side-on mode with both the head and tail of GenX bound to the mixed phases. It is noteworthy that the observed no-effect of pH on adsorption could also be due to the very high removal of GenX in all cases. Our goal here was to show that 3% Bi/TNTs@AC was able to effectively concentrate GenX over a broad pH range at practically relevant dosages.

Thus, the photodegradation efficiency of GenX is evaluated at the five different pH values (Fig. 5b). The 4-h GenX photodegradation showed a clear decreasing trend with increasing pH, from 78.4% at pH 3.5 to 76.4%, 74.1%, 68.0%, and 44.8% at pH 5.0, 7.0, 8.5, and 10.0, respectively. Apparently, the photodegradation effectiveness is associated with the adsorption modes of GenX. As to be illustrated in Sections 3.7 and 3.8, the head group decarboxylation is a critical step in the GenX degradation process. As such, the head-on or side-on adsorption mode is

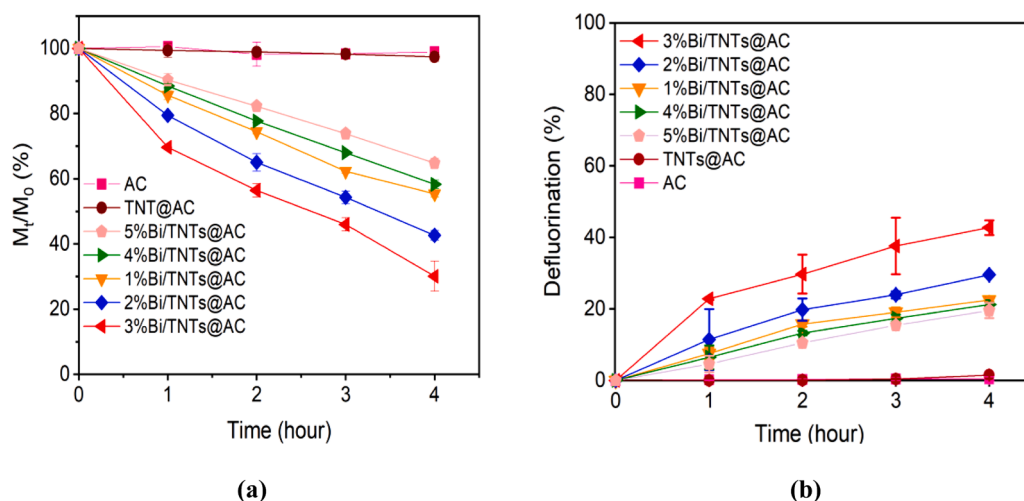


Fig. 4. (a) Photodegradation and (b) defluorination kinetics of GenX pre-adsorbed on treated AC, TNTs@AC, and Bi/TNTs@AC prepared with 1–5 wt.% Bi. Experimental conditions during adsorption–Initial GenX concentration = 100 $\mu\text{g/L}$, material dosage = 1 g/L, pH = 7.0 ± 0.1 ; Conditions for photodegradation–UV intensity = 210 W/m^2 , pH = 7.0 ± 0.1 . Data are plotted as mean of duplicates with error bars indicating relative deviation from the mean.

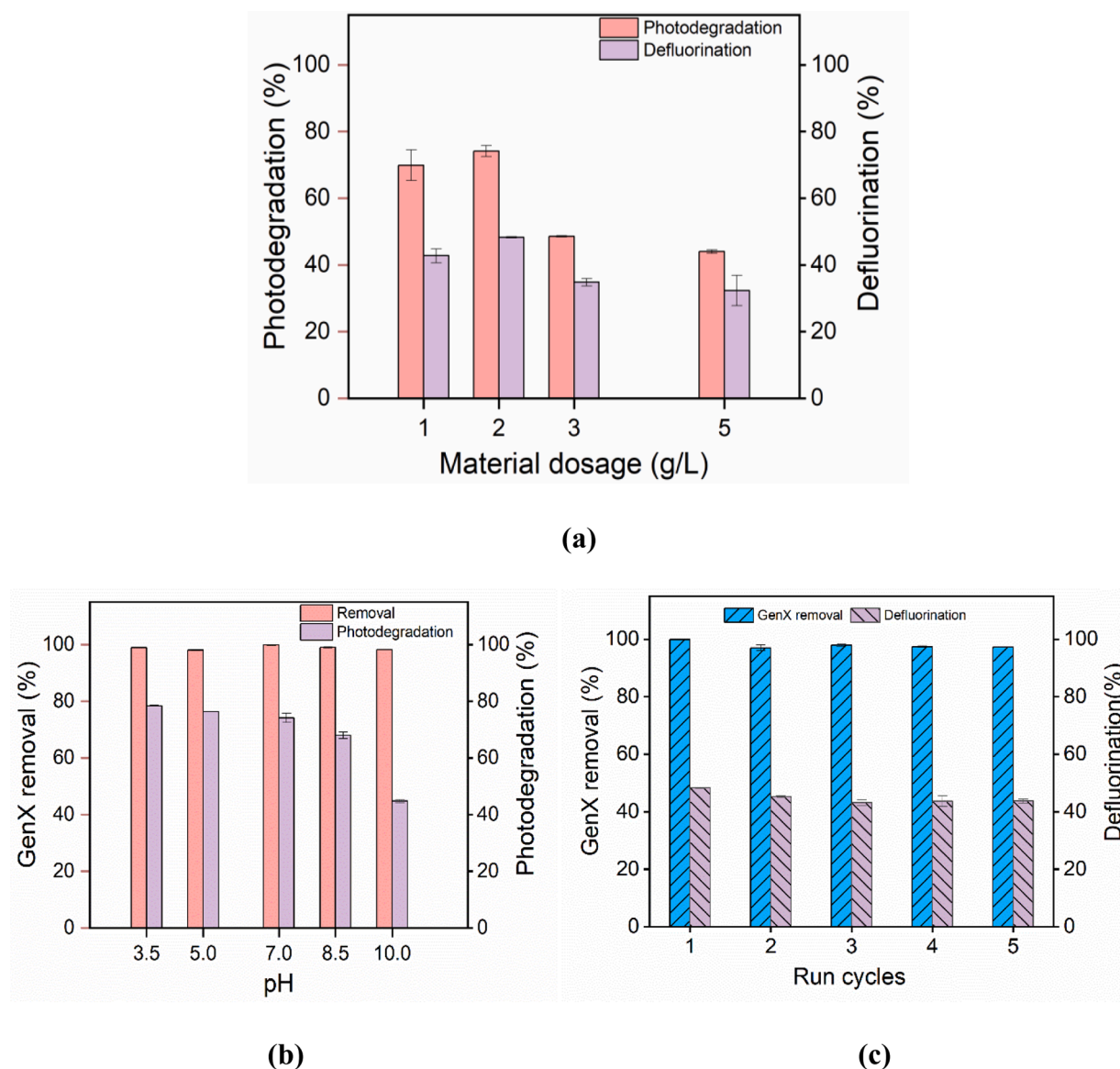


Fig. 5. (a) Photodegradation and defluorination of GenX pre-sorbed on 3%Bi/TNTs@AC at various material dosages of 1-5 g/L during adsorption; (b) effect of pH on GenX adsorption and photodegradation by 3%Bi/TNTs@AC; and (c) adsorption and solid-phase defluorination of GenX during five consecutive cycles using the same 3%Bi/TNTs@AC. Experimental conditions (adsorption)—Initial GenX concentration = 100 µg/L, material dosage = 2 g/L in (a) and (c) or 1 g/L in (b), adsorption time = 2 h, and pH = 7.0 ± 0.1 in (a) and (c); Experimental conditions (photodegradation)—Material dosage = 2 g/L during adsorption, UV intensity = 210 W/m², reaction time = 4 h, pH = 7.0 ± 0.1.

more favorable than the vertical tail-on mode for the photo-generated holes and radicals to attack both the head and tail groups of a GenX molecule. In addition, the production of photogenerated holes and radicals can be suppressed under alkaline conditions. Excessively high HO⁻ could react with photogenerated holes to produce excessive [•]OH, which inhibit the direct hole oxidation of GenX (Section 3.7) (Li et al. 2020a). Moreover, acidic conditions are favorable for formation of HO₂[•], which is a precursor of H₂O₂ and [•]OH (Eq. 6) (Song et al. 2012).



3.6. Stability and reusability of Bi/TNTs@AC

The efficient photodegradation of sorbed GenX was expected to automatically regenerate the material for repeated uses. To test this hypothesis, 3%Bi/TNTs@AC was subjected to five consecutive cycles of adsorption and photodegradation. After the fifth cycle, 3%Bi/TNTs@AC was still able to adsorb >98% of the GenX from solution (Fig. 5c),

indicating that the material retained its adsorption capacity. In addition, the GenX mineralization efficiency only exhibited a modest decrease from 48.3% to 43.7% after the five cycles, potentially due to competition from accumulated short-chain intermediates produced in previous cycles. No loss in Ti content was detected and <1.0 wt.% of the doped Bi leached into the solution after the five cycles.

3.7. Mechanisms of enhanced GenX photodegradation by Bi/TNTs@AC

To understand the roles of common reactive species, photocatalytic degradation experiments were carried out in the presence of radical scavengers, namely ISA for ([•]OH, BQ for O₂^{•-}, EDTA for the photo-generated h⁺, and NaN₃ for ¹O₂. Fig. 6a shows the 4-h photodegradation efficiency for GenX in the presence of variable concentrations (0.5, 1, 5, and 10 mM) of ISA, NaN₃, BQ, or EDTA. NaN₃ and BQ showed only modest or negligible effects on the photodegradation, indicating that neither O₂^{•-} nor ¹O₂ reacted with GenX. In contrast, the photodegradation decreased from 74.1% without a scavenger to 43.0%

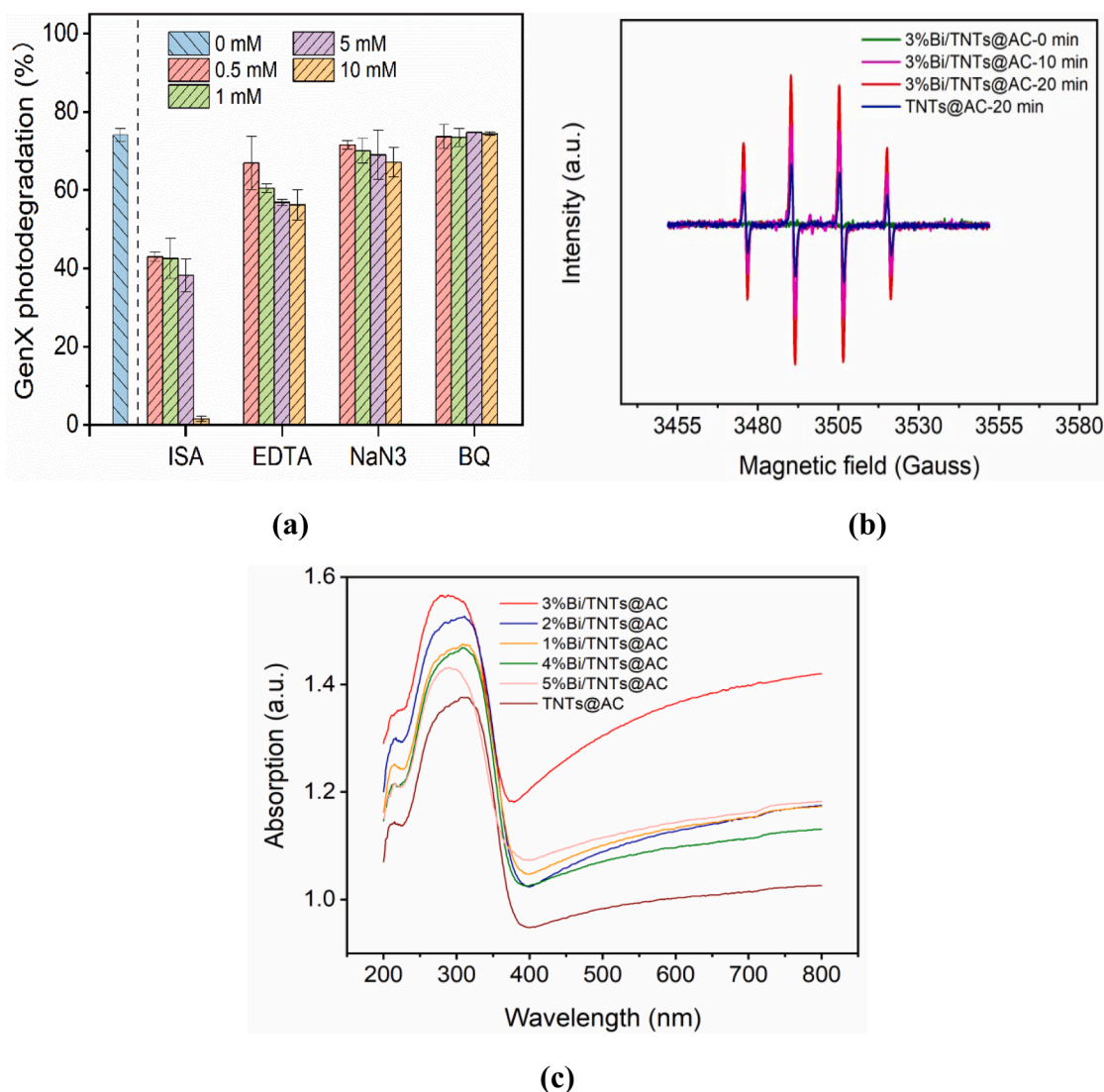


Fig. 6. (a) Photodegradation of GenX pre-sorbed on 3%Bi/TNTs@AC in the presence of a scavenger (i.e., ISA, EDTA, NaN₃, or BQ); (b) EPR spectra of DMPO-•OH adducts produced by TNTs@AC upon UV irradiation for 20 min and by 3%Bi/TNTs@AC after variable UV irradiation times; and (c) UV-DRS spectra of TNTs@AC and 3%Bi/TNTs@AC. Experimental conditions (adsorption)—Initial GenX = 100 µg/L, material dosage = 2 g/L, adsorption time = 2 h, and pH = 7.0 ± 0.1; Experimental conditions (photodegradation)—UV intensity = 210 W/m², reaction time = 4 h, pH = 7.0 ± 0.1, scavenger = 0.5, 1, 5, and 10 mM in (a), DMPO = 20 mM in (b).

in the presence of 0.5 mM ISA, and to < 1.5% when the ISA concentration was increased to 10 mM, indicating that •OH played a critical role in the photodegradation process. The addition of 0.5–10 mM of EDTA lowered the GenX degradation to 66.9%–56.2%, suggesting that h^+ also played an important role.

Fig. 6b compares the EPR spectra of DMPO-•OH adducts generated in the TNTs@AC and 3%Bi/TNTs@AC systems after 10 and 20 min of UV irradiation. A weaker •OH signal (four lines with an intensity ratio of nearly 1:2:2:1) was observed for TNTs@AC, while a stronger •OH signal was evident after the incorporation of 3 wt.% Bi on TNTs@AC. The •OH signal intensity increased with the irradiation time (Fig. 6b) due to the resulting •OH. No O₂^{•−} or ¹O₂ signals were detected for 3%Bi/TNTs@AC (Figs. S9a and S9b). The results confirmed the findings from the radical-quenching experiments (Fig. 6a).

Fig. 6c compares the optical properties of TNTs@AC and Bi/TNTs@AC with 1–5 wt.% Bi. Bi/TNTs@AC exhibited greater light absorption than TNTs@AC throughout the UV and visible ranges (200–800 nm), though TNTs@AC did demonstrate notable light absorbance due to the carbon (Kakavandi et al. 2019; Velasco-Arias et al. 2012). In particular, the maximum absorbance (285 nm) for 3%Bi/TNTs@AC was 14% higher than that (310 nm) for TNTs@AC. These results confirmed

that the Bi particles on the surface enhanced light harvesting, leading to enhanced photogeneration of electrons and holes.

This phenomenon is attributed to the SPR effect endowed by the metallic Bi on TNTs@AC. Dong et al. (2015) showed that the electromagnetic field distribution of Bi spheres reached its maximum at the surface of metallic Bi particles, and they observed that the SPR property of Bi could markedly enhance visible light harvesting and charge separation. When the surface plasmon wave interacts with a local particle or rough surface, some of the energy can be re-emitted as light. Other studies have also demonstrated that Bi particles display strong SPR effects in the UV range (228–280 nm), depending on their particle size and shape (Dong et al. 2014b; Ma et al. 2013; Wang et al. 2005). For instance, Ma et al. (2013) determined two SPR absorption peaks at 228 nm and 256 nm for mixed plate-like (40–70 nm) and polyhedral (500 nm) Bi nanocrystals. Wang et al. (2005) synthesized stabilized bismuth nanoparticles (~10 nm) that showed a surface plasmon absorption peak at 281 nm. Moreover, 3%Bi/TNTs@AC also exhibited enhanced visible light absorption, which is in agreement with previous reports that Bi displayed SPR effect in both ultraviolet and visible light domains (Sun et al. 2015; Sun et al. 2017).

PL emission intensity has been used to measure the recombination of

photo-induced electrons and holes. **Fig. S10** shows the PL emission spectra of TNTs@AC and 3%Bi/TNTs@AC. While the PL intensity for TNTs@AC included two large peaks, the spectra for 3%Bi/TNTs@AC was almost flat, indicating that deposition of Bi resulted in a remarkable decline in the recombination of electron-hole pairs. This observation agrees with the notion that metallic Bi can serve as an effective electron trap and, thus, facilitate electron-hole separation (Dong et al. 2014a). Chen et al. (2017) prepared Bi@Bi₂O₃ core-shell nanoparticles and found that metallic Bi nanoparticles can generate charge carriers due to the SPR effect, while the amorphous Bi₂O₃ surface layer serves as an efficient electron and hole acceptor to guide the directional transfer of photo-charges and enhance the separation of electron-hole pairs. The Bi₂O₃ shell could also protect the metallic Bi core from oxidation, which not only preserves the reactive lifetime, but also provides a safe environment for photocatalytic reactions (Chen et al. 2017).

Based on the experimental results and material characterization, **Fig. 7** illustrates the key mechanisms governing the enhanced adsorption and photocatalytic degradation of GenX by Bi/TNTs@AC. First, the incorporation of Bi nanoparticles on Bi/TNTs@AC creates a more favorable environment for adsorption due to suppression of the surface negative potential. The surface Bi along with Ti also serves as a Lewis acid to bind with the carboxylate group of GenX anions, which is conducive to the decarboxylation reaction that is often an essential step for PFAS degradation (Zhu et al. 2021). Second, the Bi nanoparticles enhance light absorbance (**Fig. 6c**), favoring the production of photo-generated electrons and holes. Third, due to photo-induced SPR, the metallic Bi is photoexcited and promotes excitation of surface electrons, generation of more charge carriers, and interfacial electron transfer (Chen et al. 2017). Fourth, because the Fermi level (vs NHE) of metallic Bi (-0.17 eV) (Dong et al. 2015) is lower than the conduction band (CB) level of TNTs@AC (0.12 eV) (Dang et al. 2020), the photoexcited electrons tend to flow from Bi to TNTs@AC, decreasing the recombination rate of electron-hole pairs and increasing the lifetime of charge-carriers in TNTs@AC. Fifth, the electron release results in positively charged Biⁿ⁺, which attract and trap photoexcited electrons from the valence band (VB) of TNTs@AC to maintain charge neutrality (Dong et al.

2014a), further inhibiting e^-/h^+ recombination and leaving more holes available for reacting with GenX. Lastly, the local electromagnetic field representing the SPR effects of Bi metal can also enhance the generation of electron-hole pairs and subsequent separation of the charge carriers (Tu et al. 2015). Afterwards, the separated electrons will reduce O₂ to H₂O₂ because the redox potential of O₂/H₂O₂ (0.695 eV) (Moon et al. 2017) is more positive than that of the CB of TNTs@AC, and subsequently, H₂O₂ is transformed into $\cdot\text{OH}$ by trapping an electron (Dong et al. 2014a). Given the redox potential of O₂/O₂⁻ (-0.33 eV), the CB electrons are less likely to react with O₂ (Dong et al. 2014a). Conversely, the holes with a redox potential of 3.85 eV can facilitate decarboxylation of GenX and oxidation of HO⁻ into $\cdot\text{OH}$ radicals ($E^0 = 1.99$ eV for OH⁻/ $\cdot\text{OH}$) (Dong et al. 2014a). As $\cdot\text{OH}$ radicals and h^+ are the major reactive species, the photocatalytic degradation of GenX adsorbed on Bi/TNTs@AC was enhanced.

Fig. 8a shows the molecular structure of GenX with labeled sites. **Figs. 8b** and **8c** show the highest occupied molecule orbital (HOMO) and the lowest unoccupied molecular orbital (LUMO) of GenX, respectively, and indicate that the carboxylate group is a favorable attack site for photogenerated holes and radicals. While the gain or loss of electrons on each GenX molecule site cannot be accurately obtained (Ji et al. 2020), the condensed Fukui functions were calculated based on the natural population analysis (NPA) scheme to identify the electrophilic (f^-), nucleophilic (f^+), and radical (f^0) reactive sites in GenX (**Fig. 8d**). Based on the condensed Fukui function values of 0.3309 and 0.3273, the most reactive sites for electrophilic attack are O19 and O20, respectively, of the carboxylate group. The same sites also exhibit the highest f^0 values, namely 0.1906 and 0.1981, respectively. Therefore, the carboxylate group of GenX is most prone to the attack by the photogenerated radicals, which is in agreement with previous reports of photocatalytic degradation of long-chain PFAS (Xu et al. 2020; Zhu et al. 2021). The surface contour of f^+ for GenX indicates that C1 (0.1084) and C2 (0.1188) in the CF₃CF₂CF₂- end group are most vulnerable to nucleophilic attack. This observation agrees with the report by Bao et al. (2018). However, Bao et al. (2018) also proposed that the optimal trajectory for radicals to attack the carboxyl group of GenX is blocked by -CF₃ due to steric hindrance. Pica et al. (2019) asserted that $\cdot\text{OH}$ attack on the ether bond of GenX is kinetically unfavorable because of the high activation barrier (321 kJ/mol), though the attack can result in concurrent decarboxylation. While the initial oxidative attack does not break the ether bond, stepwise mineralization can occur along the acidic side chain. Moreover, the ether bond introduces a weak point in the perfluorinated carbon chain, facilitating degradation by hydrated electrons.

3.8. Pathways of GenX photodegradation by Bi/TNTs@AC

Fig. S11 shows the chromatograms of two major stable intermediate products, TFA (CF₃COOH) and PFA (C₂F₅COOH), detected after the 4 h photocatalytic degradation of GenX by 3%Bi/TNTs@AC. Other intermediates were either unstable or unidentifiable. Taken together the mechanism analysis, reactive species quenching data, DFT calculations, intermediates, and findings from recent studies (Bao et al. 2018; Pica et al. 2019; Vakili et al. 2021), the photodegradation of GenX by 3% Bi/TNTs@AC may occur along two possible pathways (**Fig. 9**). The first pathway starts with decarboxylation by $\cdot\text{OH}$ and/or h^+ to generate an activated intermediate (C₅F₁₁O \cdot). Then, the C₅F₁₁O \cdot radical interacts with $\cdot\text{OH}$ and/or H₂O to form unstable C₃F₇OCF₃CFOH, which subsequently transforms into C₃F₇OCOF after elimination of a CF₃ moiety on the α carbon (Pica et al. 2019). Upon further reaction with $\cdot\text{OH}$, C₃F₇OCOF converts into C₄F₈HO \cdot and subsequently generates CF₃CF₂CF₂O \cdot through cleavage of the FCOOH moiety. Finally, CF₃CF₂CF₂O \cdot continues to lose the CF₂O groups until complete mineralization (Pica et al. 2019; Vakili et al. 2021).

The second pathway is initiated by reduction of the ether group by photogenerated electrons to form C₃F₇ \cdot and $\cdot\text{C}_3\text{F}_4\text{O}_3^-$ fragments. The

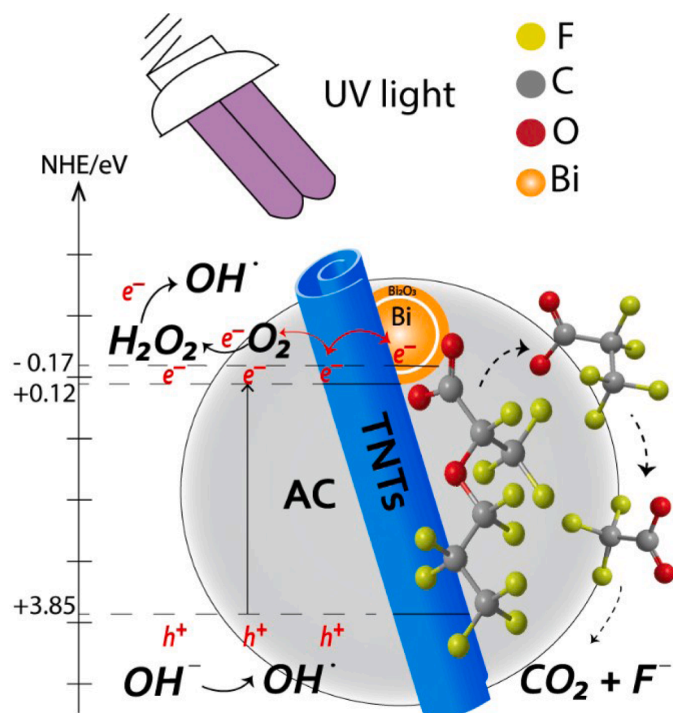


Fig. 7. Conceptualized representation of the adsorptive photocatalysis mechanism with Bi/TNTs@AC for GenX degradation under UV irradiation.

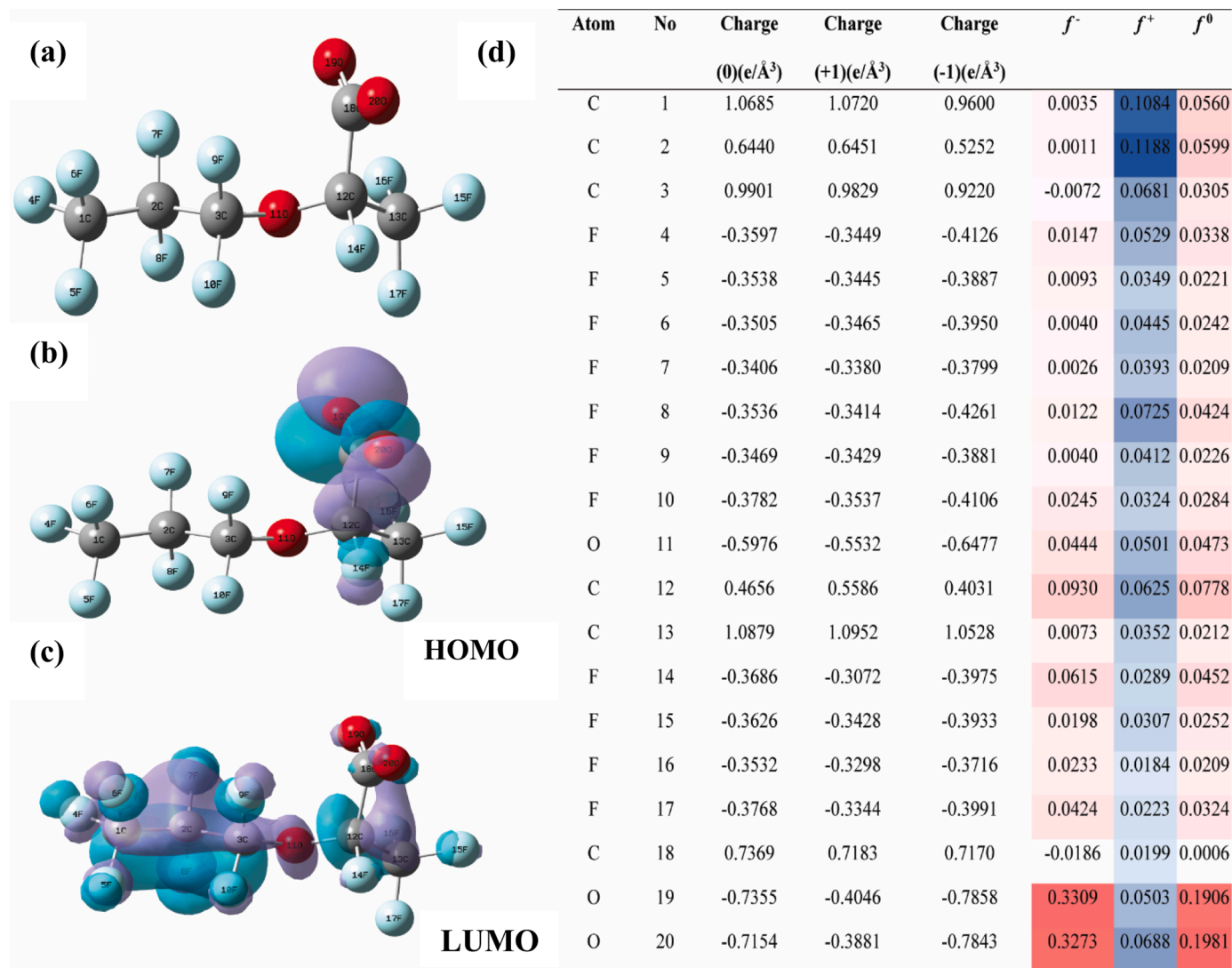


Fig. 8. (a) NPA analysis of reactive sites in a GenX molecule at the B3LYP/6–31+G(d,p) level; molecular orbitals of GenX structure showing the (b) HOMO and (c) LUMO; and (d) condensed Fukui index distribution of active sites on GenX. Green–Negative phase; Purple–Positive phase; Blue–F; Deep grey–C; Red–O.

carboxylate fragment ($\bullet\text{C}_3\text{F}_4\text{O}_3^-$) is degraded in a similar manner as pathway (1). Specifically, the carboxylate group is cleaved, and the active intermediate reacts with $\bullet\text{OH}$ and/or H_2O to form the unstable $\text{C}_2\text{F}_4\text{OOH}^-$, which is converted to $\text{C}_2\text{F}_4\text{O}$ after one H_2O molecule is eliminated. Then, $\text{C}_2\text{F}_4\text{O}$ is hydrolyzed to CF_3COO^- (TFA) with the expulsion of H^+ and F^- . The $\text{C}_3\text{F}_7\bullet$ fragment may react with $\bullet\text{OH}$ or H_2O to generate unstable $\text{C}_3\text{F}_7\text{OH}$, which further transforms into $\text{CF}_3\text{CF}_2\text{COF}$. Upon hydrolysis, $\text{CF}_3\text{CF}_2\text{COF}$ converts into $\text{C}_2\text{F}_5\text{COO}^-$ (PFA), which is converted into $\text{C}_2\text{F}_5\text{OH}$ upon decarboxylation by $\bullet\text{OH}$ and h^+ (Niu et al. 2012). The unstable alcohol undergoes intramolecular rearrangement to form CF_3COF and converts into CF_3COO^- (Niu et al. 2012). In addition, electrons may attack other fluorine atoms in the fluorocarbon tail (Park et al. 2009; Song et al. 2013), resulting in an alternative pathway for PFA photodegradation, where PFA is transformed into $\text{CF}_3\text{CH}_2\text{COO}^-$ via $\text{H}^\bullet/\text{F}$ exchange and subsequently converted into CF_3COO^- upon elimination of a $\bullet\text{CH}_2$ moiety (Bao et al. 2018; Park et al. 2009; Song et al. 2013). The TFA generated from decomposition of the two GenX fragments may be further degraded to $\bullet\text{CF}_3$ and $\bullet\text{COO}^-$. The resulting $\bullet\text{CF}_3$ may combine with other radicals (e.g., $\bullet\text{CF}_3$ or HO^\bullet) to form gaseous products (e.g., CF_3H , C_2F_6) (Bao et al. 2018).

4. Conclusions

A new adsorptive photocatalyst was prepared, characterized, and tested for degradation of GenX as a model emerging PFAS. The major findings are summarized as follows:

- 1) The most reactive Bi/TNTs@AC was prepared by depositing 3 wt.% Bi on AC-supported titanate nanotubes constructed with commercially available AC and P25.
- 2) Material characterization indicated that Bi was deposited on the material surface as nanoparticles with a metallic Bi core and amorphous Bi_2O_3 shell. In addition, micro- or nanoscale AC particles were also observed on TNTs.
- 3) Bi/TNTs@AC was able to adsorb nearly all GenX in 1 h, effectively concentrating GenX on the photoactive sites. Subsequently, 70.0% of the pre-sorbed GenX was degraded, including 42.7% defluorinated, after 4 h of UV irradiation. The photodegradation process also regenerated the material, enabling repeated uses without additional chemical regeneration.
- 4) The hybrid Bi, anatase, and AC phases at the microscale or nanoscale facilitated enhanced adsorption of GenX through concurrent and synergistic hydrophobic, Lewis acid-base, and anion- π interactions.

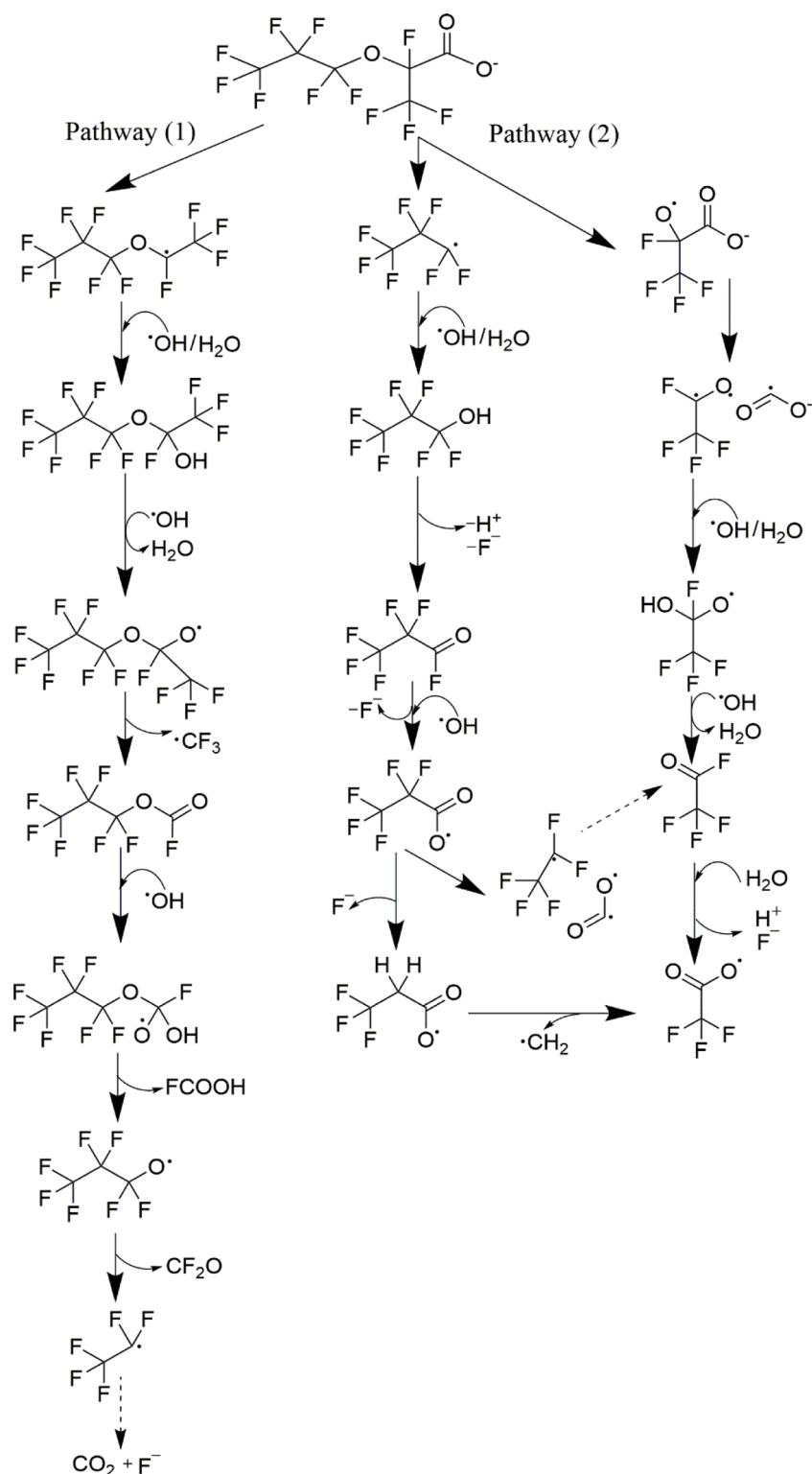


Fig. 9. Proposed photodegradation pathways of GenX by 3%Bi/TNTs@AC under UV irradiation.

- 5) The SPR effect enabled by the metallic Bi nanoparticles greatly enhanced light harvesting, generation of charge carriers, and separation of e^-/h^+ pairs.
- 6) While DFT findings suggested that the carboxylate group was the prone to the radical attack in the UV system, the ether bond was a favorable attack site for photogenerated electrons.
- 7) $\cdot\text{OH}$ radicals and photogenerated h^+ were the main reactive species for the photocatalytic degradation of GenX by Bi/TNTs@AC, which

starts with cleavage of the carboxylate group, conversion to $\text{CF}_3\text{CF}_2\text{CF}_2\text{O}\cdot$ via decarboxylation and CF_3 elimination, and continues through sequential loss of CF_2O groups until complete mineralization. In addition, the ether bond in the GenX molecule may be attacked by photogenerated electrons, opening up another degradation pathway.

Given the widespread use of GenX as a substitute for legacy PFAS and

the growing health concerns, Bi/TNTs@AC and the concentrate-and-destroy concept may serve as an important technology for cost-effective treatment of GenX-contaminated waters.

CRedit authorship contribution statement

Yangmo Zhu: Conceptualization, Methodology, Software, Formal analysis, Investigation, Data curation, Writing – original draft, Visualization. **Haodong Ji:** Funding acquisition. **Ke He:** Data curation, Writing – review & editing. **Lee Blaney:** Data curation, Writing – review & editing. **Tianyuan Xu:** Methodology, Validation, Formal analysis, Resources, Writing – review & editing, Supervision. **Dongye Zhao:** Funding acquisition, Conceptualization, Methodology, Validation, Resources, Writing – review & editing, Supervision.

Declaration of Competing Interest

The authors declare that they have no known competing financial interests or personal relationships that could have appeared to influence the work reported in this paper.

Acknowledgments

We gratefully acknowledge financial support from the Strategic Environmental Research and Development Program (SERDP) (ER18-1515), the National Science Foundation (CBET-2041060), and the Alabama Research & Development Fund (1ARDEF20 01).

Supplementary materials

Supplementary material associated with this article can be found, in the online version, at doi:[10.1016/j.watres.2022.118650](https://doi.org/10.1016/j.watres.2022.118650).

References

- Ahmadpour, N., Sayadi, M.H., Homaieghar, S., 2020. A hierarchical Ca/TiO₂/NH₂-MIL-125 nanocomposite photocatalyst for solar visible light induced photodegradation of organic dye pollutants in water. *RSC Adv.* 10 (50), 29808–29820. <https://doi.org/10.1039/D0RA05192F>.
- Almeida, R.M., Vasconcelos, H.C., Goncalves, M.C., Santos, L.F., 1998. XPS and NEXAFS studies of rare-earth doped amorphous sol–gel films. *J. Non-Cryst. Solids* 232, 65–71. [https://doi.org/10.1016/S0022-3093\(98\)00545-6](https://doi.org/10.1016/S0022-3093(98)00545-6).
- Bao, Y., Deng, S., Jiang, X., Qu, Y., He, Y., Liu, L., Chai, Q., Mumtaz, M., Huang, J., Cagnetta, G., Yu, G., 2018. Degradation of PFOA substitute–GenX (HFPO-DA ammonium salt)–Oxidation with UV/persulfate or reduction with UV/sulfite? *Environ. Sci. Technol.* 52 (20), 11728–11734. <https://doi.org/10.1021/acs.est.8b02172>.
- Brandsma, S.H., Koekkoek, J.C., van Velzen, M.J.M., de Boer, J., 2019. The PFOA substitute GenX detected in the environment near a fluoropolymer manufacturing plant in the Netherlands. *Chemosphere* 220, 493–500. <https://doi.org/10.1016/j.chemosphere.2018.12.135>.
- Cai, Z., Zhao, X., Wang, T., Liu, W., Zhao, D., 2017. Reusable platinum-deposited anatase/hexa-titanate nanotubes–Roles of reduced and oxidized platinum on enhanced solar-light-driven photocatalytic activity. *ACS Sustain. Chem. Eng.* 5 (1), 547–555. <https://doi.org/10.1021/acssuschemeng.6b01931>.
- Chen, M., Li, Y., Wang, Z., Gao, Y., Huang, Y., Cao, J., Ho, W., Lee, S., 2017. Controllable synthesis of core–shell Bi@amorphous Bi₂O₃ nanospheres with tunable optical and photocatalytic activity for NO removal. *Ind. Eng. Chem. Res.* 56 (37), 10251–10258. <https://doi.org/10.1021/acs.iecr.7b02497>.
- Christensen, E.R., Zhang, R., Codling, G., Giesy, J.P., Li, A., 2019. Poly-and perfluoroalkyl compounds in sediments of the Laurentian Great Lakes–Loadings, temporal trends, and sources determined by positive matrix factorization. *Environ. Pollut.* 255, 113166. <https://doi.org/10.1016/j.envpol.2019.113166>.
- Cui, Q., Pan, Y., Zhang, H., Sheng, N., Wang, J., Guo, Y., Dai, J., 2018. Occurrence and tissue distribution of novel perfluoroether carboxylic and sulfonic acids and legacy per/polyfluoroalkyl substances in black-spotted frog (*Pelophylax nigromaculatus*). *Environ. Sci. Technol.* 52 (3), 982–990. <https://doi.org/10.1021/acs.est.7b03662>.
- Dang, C., Sun, F., Jiang, H., Huang, T., Liu, W., Chen, X., Ji, H., 2020. Pre-accumulation and in-situ destruction of diclofenac by a photo-regenerable activated carbon fiber supported titanate nanotubes composite material–Intermediates, DFT calculation, and ecotoxicity. *J. Hazard. Mater.* 400, 123225. <https://doi.org/10.1016/j.jhazmat.2020.123225>.
- DEQ, North Carolina Department of Environmental Quality. 2018. DEQ GenX update house select committee on North Carolina River Quality. <https://www.ncleg.gov/documents/sites/committees/house2017-185/Meetings/7%20-%20April%2026%202018/DEQ%20Update%20on%20GenX.pdf>.
- Ding, S., Niu, J., Bao, Y., Hu, L., 2013. Evidence of superoxide radical contribution to demineralization of sulfamethoxazole by visible-light-driven Bi₂O₃/Bi₂O₂CO₃/Sr₆Bi₂O₉ photocatalyst. *J. Hazard. Mater.* 262, 812–818. <https://doi.org/10.1016/j.jhazmat.2013.09.048>.
- Dixit, F., Barbeau, B., Mostafavi, S.G., Mohseni, M., 2021. PFAS and DOM removal using an organic scavenger and PFAS-specific resin–Trade-off between regeneration and faster kinetics. *Sci. Total Environ.* 754, 142107. <https://doi.org/10.1016/j.scitotenv.2020.142107>.
- Dong, F., Li, Q., Sun, Y., Ho, W., 2014a. Noble metal-like behavior of plasmonic Bi particles as a cocatalyst deposited on (BiO)₂CO₃ microspheres for efficient visible light photocatalysis. *ACS Catal.* 4 (12), 4341–4350. <https://doi.org/10.1021/cs501038q>.
- Dong, F., Xiong, T., Sun, Y., Zhao, Z., Zhou, Y., Feng, X., Wu, Z., 2014b. A semimetal bismuth element as a direct plasmonic photocatalyst. *Chem. Commun.* 50 (72), 10386–10389. <https://doi.org/10.1039/C4CC02724H>.
- Dong, F., Zhao, Z., Sun, Y., Zhang, Y., Yan, S., Wu, Z., 2015. An advanced semimetal-organic Bi spheres-g-C₃N₄ nanohybrid with SPR-enhanced visible-light photocatalytic performance for NO purification. *Environ. Sci. Technol.* 49 (20), 12432–12440. <https://doi.org/10.1021/acs.est.5b03758>.
- Duan, L., Wang, B., Heck, K., Guo, S., Clark, C.A., Arredondo, J., Wang, M., Senfite, T.P., Westerhoff, P., Wen, X., 2020. Efficient photocatalytic PFOA degradation over boron nitride. *Environ. Sci. Technol. Lett.* 7 (8), 613–619. <https://doi.org/10.1021/acs.estlett.0c00434>.
- El-Sheikh, S.M., Khedr, T.M., Hakki, A., Ismail, A.A., Badawy, W.A., Bahnmann, D.W., 2017. Visible light activated carbon and nitrogen co-doped mesoporous TiO₂ as efficient photocatalyst for degradation of ibuprofen. *Sep. Purif. Technol.* 173, 258–268. <https://doi.org/10.1016/j.seppur.2016.09.034>.
- EPA 2016a. Drinking water health advisory for perfluorooctane sulfonate (PFOS). https://www.epa.gov/sites/default/files/2016-05/documents/pfos_health_advisory_final-plain.pdf.
- EPA 2016b. Drinking water health advisory for perfluorooctanoic acid (PFOA). https://www.epa.gov/sites/default/files/2016-05/documents/pfoa_health_advisory_final-plain.pdf.
- Gebbink, W.A., van Asseldonk, L., van Leeuwen, S.P.J., 2017. Presence of emerging per- and polyfluoroalkyl substances (PFASs) in river and drinking water near a fluorochemical production plant in the Netherlands. *Environ. Sci. Technol.* 51 (19), 11057–11065. <https://doi.org/10.1021/acs.est.7b02488>.
- Gomis, M.I., Vestergren, R., Borg, D., Cousins, I.T., 2018. Comparing the toxic potency in vivo of long-chain perfluoroalkyl acids and fluorinated alternatives. *Environ. Int.* 113, 1–9. <https://doi.org/10.1016/j.envint.2018.01.011>.
- Gopiraman, M., Saravanamoorthy, S., Kim, S., Chung, I., 2017. Interconnected meso-/microporous carbon derived from pumpkin seeds as an efficient electrode material for supercapacitors. *Carbon Lett.* 24, 73–81. <https://doi.org/10.5714/CL.2017.24.73>.
- Herkert, N.J., Merrill, J., Peters, C., Bollinger, D., Zhang, S., Hoffman, K., Ferguson, P.L., Knappe, D.R.U., Stapleton, H.M., 2020. Assessing the effectiveness of point-of-use residential drinking water filters for perfluoroalkyl substances (PFASs). *Environ. Sci. Technol. Lett.* 7 (3), 178–184. <https://doi.org/10.1021/acs.estlett.0c00004>.
- Heydebreck, F., Tang, J., Xie, Z., Ebinghaus, R., 2015. Alternative and legacy perfluoroalkyl substances–Differences between European and Chinese river/estuary systems. *Environ. Sci. Technol.* 49 (24), 14742–14743. <https://doi.org/10.1021/acs.est.5b01648>.
- The Hill. 2021. EPA finds chemical contaminating NC river more toxic than previously assessed. <https://thehill.com/policy/energy-environment/578339-epa-finds-chemical-contaminating-nc-river-more-toxic-than-rl-1>.
- Ji, H., Du, P., Zhao, D., Li, S., Sun, F., Duin, E.C., Liu, W., 2020. 2D/1D graphitic carbon nitride/titanate nanotubes heterostructure for efficient photocatalysis of sulfamethazine under solar light–Catalytic “hot spots” at the rutile–anatase–titanate interfaces. *Appl. Catal. B* 263, 118357. <https://doi.org/10.1016/j.apcatb.2019.118357>.
- Kakavandi, B., Bahari, N., Kalantary, R.R., Fard, E.D., 2019. Enhanced sono-photocatalysis of tetracycline antibiotic using TiO₂ decorated on magnetic activated carbon (MAC@T) coupled with US and UV–A new hybrid system. *Ultrason. Sonochem.* 55, 75–85. <https://doi.org/10.1016/j.ultsonch.2019.02.026>.
- Khan, M.U., Siddiqui, Z.N., 2021. Niobia supported sulfated bismuth oxide nanorods (S-Bi₂O₃@Nb₂O₅)–Acidic properties, catalytic activity and green metrics analysis. *Sustain. Chem. Pharm.* 24, 100542. <https://doi.org/10.1016/j.scp.2021.100542>.
- Lan, Y., Li, Z., Li, D., Xie, W., Yan, G., Guo, S., 2020. Visible-light responsive Z-scheme Bi@β-Bi₂O₃/g-C₃N₄ heterojunction for efficient photocatalytic degradation of 2, 3-dihydroxynaphthalene. *Chem. Eng. J.* 392, 123686. <https://doi.org/10.1016/j.cej.2019.123686>.
- Lee, C.K., Wang, C.C., Lyu, M.D., Juang, L.C., Liu, S.S., Hung, S.H., 2007. Effects of sodium content and calcination temperature on the morphology, structure and photocatalytic activity of nanotubular titanates. *J. Colloid Interface Sci.* 316, 562–569. <https://doi.org/10.1016/j.jcis.2007.08.008>.
- Lenka, S.P., Kah, M., Padhye, L.P., 2021. A review of the occurrence, transformation, and removal of poly-and perfluoroalkyl substances (PFAS) in wastewater treatment plants. *Water Res.* 199, 117187. <https://doi.org/10.1016/j.watres.2021.117187>.
- Li, F., Wei, Z., He, K., Blaney, L., Cheng, X., Xu, T., Liu, W., Zhao, D., 2020a. A concentrate-&-destroy technique for degradation of perfluorooctanoic acid in water using a new adsorptive photocatalyst. *Water Res.* 185, 116219. <https://doi.org/10.1016/j.watres.2020.116219>.

- Li, Y., Ding, L., Liang, Z., Xue, Y., Cui, H., Tian, J., 2020b. Synergetic effect of defects rich MoS_2 and Ti_3C_2 MXene as cocatalysts for enhanced photocatalytic H_2 production activity of TiO_2 . *Chem. Eng. J.* 383, 123178 <https://doi.org/10.1016/j.cej.2019.123178>.
- Lindstrom, A.B., Strynar, M.J., Libelo, E.L., 2011. Polyfluorinated compounds—Past, present, and future. *Environ. Sci. Technol.* 45 (19), 7954–7961. <https://doi.org/10.1021/es2011622>.
- Liu, J., Zou, S., Wang, H., Xiao, L., Zhao, H., Fan, J., 2017. Synergistic effect between Pt^0 and $\text{Bi}_2\text{O}_{3-x}$ for efficient room-temperature alcohol oxidation under base-free aqueous conditions. *Catal. Sci. Technol.* 7 (5), 1203–1210. <https://doi.org/10.1039/C6CY02596J>.
- Liu, K., Zhang, S., Hu, X., Zhang, K., Roy, A., Yu, G., 2015. Understanding the adsorption of PFOA on MIL-101 (Cr)-based anionic-exchange metal-organic frameworks—Comparing DFT calculations with aqueous sorption experiments. *Environ. Sci. Technol.* 49 (14), 8657–8665. <https://doi.org/10.1021/acs.est.5b00802>.
- Liu, W., Cai, Z.Q., Zhao, X., Wang, T., Li, F., Zhao, D.Y., 2016. High-capacity and photoregenerable composite material for efficient adsorption and degradation of phenanthrene in water. *Environ. Sci. Technol.* 50 (20), 11174–11183. <https://doi.org/10.1021/acs.est.6b02623>.
- Ma, D., Zhao, J., Chu, R., Yang, S., Zhao, Y., Hao, X., Li, L., Zhang, L., Lu, Y., Yu, C., 2013. Novel synthesis and characterization of bismuth nano/microcrystals with sodium hypophosphite as reductant. *Adv. Powder Technol.* 24 (1), 79–85. <https://doi.org/10.1016/j.apt.2012.02.004>.
- Ma, J., Li, F., Qian, T., Liu, H., Liu, W., Zhao, D., 2017. Natural organic matter resistant powder activated charcoal supported titanate nanotubes for adsorption of Pb(II). *Chem. Eng. J.* 315, 191–200. <https://doi.org/10.1016/j.cej.2017.01.029>.
- Ma, X., Zhang, F., Wei, L., 2015. Effect of wood charcoal contents on the adsorption property, structure, and morphology of mesoporous activated carbon fibers derived from wood liquefaction process. *J. Mater. Sci.* 50 (4), 1908–1914. <https://doi.org/10.1007/s10853-014-8754-6>.
- Mantripragada, S., Deng, D., Zhang, L., 2021. Remediation of GenX from water by amidoxime surface-functionalized electrospun polyacrylonitrile nanofibrous adsorbent. *Chemosphere* 283, 131235. <https://doi.org/10.1016/j.chemosphere.2021.131235>.
- MDH, Minnesota Department of Health 2017. PFBS and Drinking Water <https://www.health.state.mn.us/communities/environment/risk/docs/guidance/gw/pfbsinfo.pdf>.
- Mirzaei, A., Yerushalmi, L., Chen, Z., Haghighat, F., Guo, J., 2018. Enhanced photocatalytic degradation of sulfamethoxazole by zinc oxide photocatalyst in the presence of fluoride ions—Optimization of parameters and toxicological evaluation. *Water Res.* 132, 241–251. <https://doi.org/10.1016/j.watres.2018.01.016>.
- Moon, G., Fujitsuka, M., Kim, S., Majima, T., Wang, X., Choi, W., 2017. Eco-friendly photochemical production of H_2O_2 through O_2 reduction over carbon nitride frameworks incorporated with multiple heteroelements. *ACS Catal.* 7 (4), 2886–2895. <https://doi.org/10.1021/acscatal.6b03334>.
- Niu, J., Lin, H., Xu, J., Wu, H., Li, Y., 2012. Electrochemical mineralization of perfluorocarboxylic acids (PFCAs) by Ce-doped modified porous nanocrystalline PbO_2 film electrode. *Environ. Sci. Technol.* 46 (18), 10191–10198. <https://doi.org/10.1021/es302148z>.
- Olvera-Vargas, H., Wang, Z., Xu, J., Lefebvre, O., 2021. Synergistic degradation of GenX (hexafluoropropylene oxide dimer acid) by pairing graphene-coated Ni-foam and boron doped diamond electrodes. *Chem. Eng. J.* 430, 132686 <https://doi.org/10.1016/j.cej.2021.132686>.
- Park, H., Vecitis, C.D., Cheng, J., Choi, W., Mader, B.T., Hoffmann, M.R., 2009. Reductive defluorination of aqueous perfluorinated alkyl surfactants—Effects of ionic headgroup and chain length. *J. Phys. Chem. A* 113 (4), 690–696. <https://doi.org/10.1021/jp807116q>. <https://pubs.acs.org/doi/pdf/10.1021/jp807116q>.
- Pica, N.E., Funkhouser, J., Yin, Y., Zhang, Z., Ceres, D.M., Tong, T., Blotvogel, J., 2019. Electrochemical oxidation of hexafluoropropylene oxide dimer acid (GenX)—Mechanistic insights and efficient treatment train with nanofiltration. *Environ. Sci. Technol.* 53 (21), 12602–12609. <https://doi.org/10.1021/acs.est.9b03171>.
- Qamar, M., Yoon, C.R., Oh, H.J., Lee, N.H., Park, K., Kim, D.H., Lee, K.S., Lee, W.J., Kim, S.J., 2008. Preparation and photocatalytic activity of nanotubes obtained from titanium dioxide. *Catal. Today* 131 (1–4), 3–14. <https://doi.org/10.1016/j.cattod.2007.10.015>.
- Rahman, M.F., Peldszus, S., Anderson, W.B., 2014. Behaviour and fate of perfluoroalkyl and polyfluoroalkyl substances (PFASs) in drinking water treatment—A review. *Water Res.* 50, 318–340. <https://doi.org/10.1016/j.watres.2013.10.045>.
- Razali, M.H., Mohd Noor, A.-F., Mohamed, A.R., Sreekantan, S., 2012. Morphological and structural studies of titanate and titania nanostructured materials obtained after heat treatments of hydrothermally produced layered titanate. *J. Nanomater.* 2012, 1–10. <https://doi.org/10.1155/2012/962073>.
- Song, C., Chen, P., Wang, C., Zhu, L., 2012. Photodegradation of perfluorooctanoic acid by synthesized TiO_2 -MWCNT composites under 365 nm UV irradiation. *Chemosphere* 86 (8), 853–859. <https://doi.org/10.1016/j.chemosphere.2011.11.034>.
- Song, Z., Dong, X., Wang, N., Zhu, L., Luo, Z., Fang, J., Xiong, C., 2017. Efficient photocatalytic defluorination of perfluorooctanoic acid over BiOCl nanosheets via a hole direct oxidation mechanism. *Chem. Eng. J.* 317, 925–934. <https://doi.org/10.1016/j.cej.2017.02.126>.
- Song, Z., Tang, H., Wang, N., Zhu, L., 2013. Reductive defluorination of perfluorooctanoic acid by hydrated electrons in a sulfite-mediated UV photochemical system. *J. Hazard. Mater.* 262, 332–338. <https://doi.org/10.1016/j.jhazmat.2013.08.059>.
- Subramaniam, M., Goh, P., Abdullah, N., Lau, W., Ng, B., Ismail, A., 2017. Adsorption and photocatalytic degradation of methylene blue using high surface area titanate nanotubes (TNT) synthesized via hydrothermal method. *J. Nanopart. Res.* 19 (6), 1–13. <https://doi.org/10.1007/s11051-017-3920-9>.
- Sun, M., Arevalo, E., Strynar, M., Lindstrom, A., Richardson, M., Kearns, B., Pickett, A., Smith, C., Knappe, D.R.U., 2016. Legacy and emerging perfluoroalkyl substances are important drinking water contaminants in the Cape Fear river watershed of North Carolina. *Environ. Sci. Technol. Lett.* 3 (12), 415–419. <https://doi.org/10.1021/acs.estlett.6b00398>.
- Sun, Y., Zhao, Z., Dong, F., Zhang, W., 2015. Mechanism of visible light photocatalytic NO_x oxidation with plasmonic Bi cocatalyst-enhanced $(\text{BiO})_2\text{CO}_3$ hierarchical microspheres. *Phys. Chem. Chem. Phys.* 17 (16), 10383–10390. <https://doi.org/10.1039/C4CP06045H>.
- Sun, Y., Zhao, Z., Zhang, W., Gao, C., Zhang, Y., Dong, F., 2017. Plasmonic Bi metal as cocatalyst and photocatalyst—The case of $\text{Bi}/(\text{BiO})_2\text{CO}_3$ and Bi particles. *J. Colloid Interface Sci.* 485, 1–10. <https://doi.org/10.1016/j.jcis.2016.09.018>.
- Sunderland, E.M., Hu, X.C., Dassuncao, C., Tokranov, A.K., Wagner, C.C., Allen, J.G., 2019. A review of the pathways of human exposure to poly- and perfluoroalkyl substances (PFASs) and present understanding of health effects. *J. Expo. Sci. Environ. Epidemiol.* 29 (2), 131–147. <https://doi.org/10.1038/s41370-018-0094-1>.
- Tu, W., Zhou, Y., Li, H., Li, P., Zou, Z., 2015. Au@ TiO_2 yolk-shell hollow spheres for plasmon-induced photocatalytic reduction of CO_2 to solar fuel via a local electromagnetic field. *Nanoscale* 7 (34), 14232–14236. <https://doi.org/10.1039/C5NR02943K>.
- Vakili, M., Bao, Y., Gholami, F., Gholami, Z., Deng, S., Wang, W., Awasthi, A.K., Rafatullah, M., Cagnetta, G., Yu, G., 2021. Removal of HFPO-DA (GenX) from aqueous solutions—A mini-review. *Chem. Eng. J.* 424, 130266 <https://doi.org/10.1016/j.cej.2021.130266>.
- Van Doorslaer, X., Heynderickx, P.M., Demeestere, K., Debever, K., Van Langenhove, H., Dewulf, J., 2012. TiO_2 mediated heterogeneous photocatalytic degradation of moxifloxacin—Operational variables and scavenger study. *Appl. Catal. B* 111, 150–156. <https://doi.org/10.1016/j.apcatb.2011.09.029>.
- Velasco-Arias, D., Zumeta-Dube, I., Díaz, D., Santiago-Jacinto, P., Ruiz-Ruiz, V.-F., Castillo-Blum, S.-E., Rendon, L., 2012. Stabilization of strong quantum confined colloidal bismuth nanoparticles, one-pot synthesized at room conditions. *J. Phys. Chem.* 116 (27), 14717–14727. <https://doi.org/10.1021/jp304170k>.
- Wang, F., Lu, X., Li, X., Shih, K.M., 2015. Effectiveness and mechanisms of defluorination of perfluorinated alkyl substances by calcium compounds during waste thermal treatment. *Environ. Sci. Technol.* 49 (9), 5672–5680. <https://doi.org/10.1021/es506234b>.
- Wang, J., Wang, X., Sheng, N., Zhou, X., Cui, R., Zhang, H., Dai, J., 2017. RNA-sequencing analysis reveals the hepatotoxic mechanism of perfluoroalkyl alternatives, HFPO2 and HFPO4, following exposure in mice. *J. Appl. Toxicol.* 37 (4), 436–444. <https://doi.org/10.1002/jat.3376>.
- Wang, N., Li, X., Yang, Y., Zhou, Z., Shang, Y., Zhuang, X., Zhang, T., 2020. Two-stage calcination composite of Bi_2O_3 - TiO_2 supported on powdered activated carbon for enhanced degradation of sulfamethazine under solar irradiation. *J. Water Process Eng.* 35, 101220 <https://doi.org/10.1016/j.jwpe.2020.101220>.
- Wang, Q., Lei, X., Pan, F., Xia, D., Shang, Y., Sun, W., Liu, W., 2018. A new type of activated carbon fibre supported titanate nanotubes for high-capacity adsorption and degradation of methylene blue. *Colloid Surf. A* 555, 605–614. <https://doi.org/10.1016/j.colsurfa.2018.07.016>.
- Wang, W., Maimaiti, A., Shi, H., Wu, R., Wang, R., Li, Z., Qi, D., Yu, G., Deng, S., 2019. Adsorption behavior and mechanism of emerging perfluoro-2-propoxypropanoic acid (GenX) on activated carbons and resins. *Chem. Eng. J.* 364, 132–138. <https://doi.org/10.1016/j.cej.2019.01.153>.
- Wang, Y., Hong, B.H., Kim, K.S., 2005. Size control of semimetal bismuth nanoparticles and the UV-visible and IR absorption spectra. *J. Phys. Chem. B* 109 (15), 7067–7072. <https://doi.org/10.1021/jp046423v>.
- Weng, S., Chen, B., Xie, L., Zheng, Z., Liu, P., 2013. Facile in situ synthesis of a Bi/ BiOCl nanocomposite with high photocatalytic activity. *J. Mater. Chem. A* 1 (9), 3068–3075. <https://doi.org/10.1039/C2TA01004F>.
- Xu, T., Ji, G., Gu, Y., Tong, T., Xia, Y., Zhang, L., Zhao, D., 2020a. Enhanced adsorption and photocatalytic degradation of perfluorooctanoic acid in water using iron (hydr) oxides/carbon sphere composite. *Chem. Eng. J.* 388, 124230 <https://doi.org/10.1016/j.cej.2020.124230>.
- Xu, T., Zhu, Y., Duan, J., Xia, Y., Tong, T., Zhang, L., Zhao, D., 2020. Enhanced photocatalytic degradation of perfluorooctanoic acid using carbon-modified bismuth phosphate composite—Effectiveness, material synergy and roles of carbon. *Chem. Eng. J.* 395, 124991 <https://doi.org/10.1016/j.cej.2020.124991>.
- Yang, B., Jiang, C., Yu, G., Zhuo, Q., Deng, S., Wu, J., Zhang, H., 2015. Highly efficient electrochemical degradation of perfluorooctanoic acid (PFOA) by F-doped Ti/SnO_2 electrode. *J. Hazard. Mater.* 299, 417–424. <https://doi.org/10.1016/j.jhazmat.2015.06.033>.
- Yang, C., Li, X., 2002. Synthesis and characterization of Ti-containing mesoporous alumina molecular sieves. *Studies in Surface Science and Catalysis*, 141. Elsevier, pp. 173–182.
- Yang, Q., Wu, Q., Liu, Y., Luo, S., Wu, X., Zhao, X., Zou, H., Long, B., Chen, W., Liao, Y., 2020. Novel Bi-doped amorphous SnO_x nanoshells for efficient electrochemical CO_2 reduction into formate at low overpotentials. *Adv. Mater.* 32 (36), 2002822 <https://doi.org/10.1002/adma.202002822>.
- Yang, Y., Ji, W., Li, X., Zheng, Z., Bi, F., Yang, M., Xu, J., Zhang, X., 2021. Insights into the degradation mechanism of perfluorooctanoic acid under visible-light irradiation

- through fabricating flower-shaped Bi₅O₇I/ZnO nn heterojunction microspheres. Chem. Eng. J. 420, 129934 <https://doi.org/10.1016/j.cej.2021.129934>.
- Zhong, b.J., Li, J.z., Lu, Y., He, X.y., Zeng, J., Hu, W., cheng Shen, Y., 2012. Fabrication of Bi³⁺-doped ZnO with enhanced photocatalytic performance. Appl. Surf. Sci. 258 (11), 4929–4933. <https://doi.org/10.1016/j.apsusc.2012.01.121>.
- Zhu, Y., Xu, T., Zhao, D., Li, F., Liu, W., Wang, B., An, B., 2021. Adsorption and solid-phase photocatalytic degradation of perfluorooctane sulfonate in water using gallium-doped carbon-modified titanate nanotubes. Chem. Eng. J. 421, 129676 <https://doi.org/10.1016/j.cej.2021.129676>.